Neurobiology of Disease

Characterization of Mice Carrying a Neurodevelopmental Disease-Associated GluN2B(L825V) Variant

Miriam Candelas Serra,[1] Viktor Kuchtiak,[1,2] Agnieszka Kubik-Zahorodna,[3] Bohdan Kysilov,[1] Klevinda Fili,[1,4] Barbora Hrcka Krausova,[1] Vera Abramova,[1,4] Mark Dobrovolski,[1,4] Karel Harant,[5] Paulina Bozikova,[6] Jiri Cerny,[1] Jan Prochazka,[3] Petr Kasparek,[3] Radislav Sedlacek,[3] Ales Balik,[1] Tereza Smejkalova,[1] and Ladislav Vyklicky[1]

[1]Institute of Physiology of the Czech Academy of Sciences, Prague 14220, Czech Republic, [2]Faculty of Science, Charles University, Prague 12800, Czech Republic, [3]Czech Centre for Phenogenomics, Institute of Molecular Genetics of the Czech Academy of Sciences, Vestec 25050, Czech Republic, [4]Third Faculty of Medicine, Charles University, Prague 10000, Czech Republic, [5]Proteomics Core Facility, Faculty of Science, Charles University, Biocev, Vestec 25050, Czech Republic, and [6]Institute of Biotechnology of the Czech Academy of Sciences, Vestec 25050, Czech Republic

N-Methyl-D-aspartate receptors (NMDARs), encoded by *GRIN* genes, are ionotropic glutamate receptors playing a critical role in synaptic transmission, plasticity, and synapse development. Genome sequence analyses have identified variants in *GRIN* genes in patients with neurodevelopmental disorders, but the underlying disease mechanisms are not well understood. Here, we have created and evaluated a transgenic mouse line carrying a missense variant *Grin2b*^{L825V}, corresponding to a de novo *GRIN2B* variant encoding GluN2B(L825V) found in a patient with intellectual disability (ID) and autism spectrum disorder (ASD). We used HEK293T cells expressing recombinant receptors and primary hippocampal neurons prepared from heterozygous *Grin2b*$^{L825V/+}$ (L825V/+) and wild-type (WT) *Grin2b*$^{+/+}$ (+/+) male and female mice to assess the functional impact of the variant. Whole-cell NMDAR currents were reduced in neurons from L825V/+ compared with +/+ mice. The peak amplitude of NMDAR-mediated evoked excitatory postsynaptic currents (NMDAR-eEPSCs) was unchanged, but NMDAR-eEPSCs in L825V/+ neurons had faster deactivation compared with +/+ neurons and were less sensitive to a GluN2B-selective antagonist ifenprodil. Together, these results suggest a decreased functional contribution of GluN2B subunits to synaptic NMDAR currents in hippocampal neurons from L825V/+ mice. The analysis of the GluN2B(L825V) subunit surface expression and synaptic localization revealed no differences compared with WT GluN2B. Behavioral testing of mice of both sexes demonstrated hypoactivity, anxiety, and impaired sensorimotor gating in the L825V/+ strain, particularly affecting males, as well as cognitive symptoms. The heterozygous L825V/+ mouse offers a clinically relevant model of *GRIN2B*-related ID/ASD, and our results suggest synaptic-level functional changes that may contribute to neurodevelopmental pathology.

Key words: autism spectrum disorder; GluN2B; mouse model; NMDA receptors; synaptic transmission

---

Significance Statement

Variants in genes for N-methyl-D-aspartate receptors (NMDARs), a subtype of ionotropic glutamate receptors, are associated with neurodevelopmental disorders. Here we have generated a transgenic mouse model of a de novo missense *GRIN2B* gene variant, identified in a patient with intellectual disability and autism, that introduces a single amino acid substitution (L825V) in the NMDAR GluN2B subunit. Di- and triheteromeric NMDARs containing the GluN2B(L825V) subunit have a reduced channel open probability. Synaptic NMDAR currents in neurons from heterozygous L825V/+ mice have accelerated deactivation and reduced ifenprodil sensitivity, suggesting synaptic loss of GluN2B function. L825V/+ mice show increased anxiety, impaired sensorimotor gating, and cognitive deficits, consistent with patient symptoms. Our study describes a clinically relevant mouse model of *GRIN2B*-related neurodevelopmental pathology.

Introduction

N-Methyl-D-aspartate receptors (NMDARs) are a subtype of ionotropic glutamate receptors important for synaptic transmission and plasticity and synaptogenesis. There are seven NMDAR genes, *GRIN1*, *GRIN2A–D*, and *GRIN3A–B*, encoding GluN1, GluN2A–B, and GluN3A–B subunits, respectively. In recent years, variants in *GRIN* genes have been identified in patients with neurodevelopmental disorders, including intellectual disability (ID), developmental delay (DD), autism spectrum disorder (ASD), schizophrenia, and epilepsy (Uzunova et al., 2014; Benke et al., 2021). Typically, the *GRIN* gene variant arises de novo in one allele of the affected gene. Most frequent are missense variants that alter the amino acid sequence of the affected subunit, and in heterologous expression systems, they are often found to influence key aspects of receptor function (Amin et al., 2021). Much less is known about how specific receptor-level functional changes contribute to neurodevelopmental pathology at the level of synaptic function or behavior.

NMDARs are heterotetramers of two obligatory GluN1 subunits and two GluN2/3 subunits, with NMDARs in principal neurons in the forebrain containing predominantly GluN2A and/or GluN2B (Hanson et al., 2024). GluN2B expression begins early during embryonic development, followed around birth by the increasing expression of GluN2A (Tovar and Westbrook, 1999). Receptors containing different combinations of GluN2 subunits have different biophysical, pharmacological, and signaling properties (Erreger et al., 2005). Compared with receptors containing GluN2A, GluN2B-containing NMDARs have a higher glutamate affinity, slower deactivation following a brief synaptic-like glutamate application, lower channel open probability (P_o), and a higher affinity for CaMKII, a key downstream signaling molecule (Hansen et al., 2021). NMDARs in the mature forebrain likely include GluN1/GluN2A/GluN2B triheteromers (Luo et al., 1997; Al-Hallaq et al., 2007; Rauner and Kohr, 2011; Tovar et al., 2013; Kellermayer et al., 2018) with functional and pharmacological properties intermediate between GluN1/GluN2A and GluN1/GluN2B diheteromers (Hansen et al., 2014; Stroebel et al., 2014, 2018). The early postnatal switch from predominantly GluN2B-containing to GluN2A-containing NMDARs (Philpot et al., 2001; Bar-Shira et al., 2015) is thought to regulate synaptic plasticity (Barria and Malinow, 2005; Dupuis et al., 2014) and synapse maturation (Hall et al., 2007; Akashi et al., 2009; Gambrill and Barria, 2011; Gray et al., 2011; Wang et al., 2011). NMDAR subunit composition thus represents a synaptic-level functional parameter that shapes the development and properties of excitatory signaling.

Consistent with a role of GluN2B in early development, mice with a homozygous deletion of the *Grin2b* gene die at birth (Kutsuwada et al., 1996). Most patients with variants in *GRIN2B* are heterozygous for their variant and present with ID/DD and ASD (Platzer et al., 2017). How different *GRIN2B* variants lead to neurodevelopmental disease is largely unknown. To our knowledge, only one patient-derived *GRIN2B* variant has been studied in a mouse model so far, the variant GluN2B(C456Y) in the agonist-binding domain (ABD; Shin et al., 2020). Here we generated a knock-in mouse line carrying a missense variant introducing a single amino acid substitution GluN2B(L825V) in the transmembrane domain (TMD) M4 helix. This variant has arisen de novo in a patient with severe ID/ASD (Awadalla et al., 2010; Tarabeux et al., 2011); thus, heterozygous animals represent a clinically relevant model. Heterologously expressed diheteromeric GluN1/GluN2B(L825V) receptors have unchanged cell surface expression, glutamate and glycine affinity, Mg^{2+} block, and H^+

sensitivity compared with GluN1/GluN2B receptors (Platzer et al., 2017; Vyklicky et al., 2018), but they show a strongly reduced P_o [Vyklicky et al., 2018; but see Amin et al. (2018)].

Here we find that even the presence of one GluN2B(L825V) subunit in triheteromeric receptors expressed in HEK293T cells reduces NMDAR P_o. Cultured hippocampal neurons from heterozygous L825V/+ mice have faster NMDAR-mediated synaptic currents that are less sensitive to a GluN2B subunit-selective inhibitor ifenprodil, suggesting a reduced functional contribution of GluN2B subunit to synaptic signaling. L825V/+ mice show sex-dependent hypoactivity, anxiety and impaired sensorimotor gating, and a cognitive deficit. Our study describes a synaptic-level manifestation of *GRIN2B*-related neurodevelopmental pathology and provides a rodent model for the future investigation of possible pharmacological or gene-editing interventions.

Materials and Methods

Ethics statement
All animals were bred and maintained according to the guidelines of the European Union Directive 2010/63/EU and approved by the Animal Care and Use Committee of the Institute of Physiology, Czech Academy of Sciences.

Animals
Mice carrying the L825V point mutation in the *Grin2b* gene that encodes the GluN2B NMDAR subunit were generated in C57BL/6N background using the CRISPR/Cas9 genome-editing system. Specific guide RNA (gRNA) recognizing exon 13 of the *Grin2b* gene (5′-GGGCGTCTTCTA TATGTTGG-3′) was designed, and off-target analyses were performed using the online software CRISPOR Design Tool (http://crispor.tefor. net/). Among the potential off-target sites identified, only one, with three mismatching nucleotides and thus low likelihood of off-target activity, is located on the same chromosome (chr6) as the *Grin2b* gene, so it could potentially be inherited within the *Grin2b* line. However, this off-target site is situated in a noncoding intergenic region. Overall the risk of off-target activity was considered minimal (Ayabe et al., 2019). Cas9 protein and gRNA with a corresponding ssDNA template (5′-AATGAGAA GAATGAGGTTATGAGCAGCCAGCTGGACATTGACAACATGGC **c**GGCGTCTTCTATATG**g**T**t**GGGGCAGCCATGGCTCTCAGCCTCA TCACCTTCATCTGTGAACATCTCTT-3′) were used for zygote electroporation. Correct genome editing was confirmed by PCR amplification in the founder mice and subsequent restriction fragment length polymorphism analysis using the NaeI enzyme that cuts at the created GC**c**GGC site. In parallel, the presence of the point mutations in individual mice [change from wild-type (WT) TTG to edited **g**T**t**] was also confirmed by direct Sanger sequencing of PCR amplicons (forward primer GAGGCAAATGGGGAAAAGCC, reverse primer GGAAGCTCTC TGGCTCACTG). Homozygotes (*Grin2b*[L825V/L825V]; L825V/L825V) were not viable and died before or shortly after birth. Heterozygotes were obtained from breeding heterozygous (*Grin2b*[L825V/+]; L825V/+) with WT (*Grin2b*^{+/+}; +/+) mice.

Molecular modeling
Homology modeling. A homology model of the tetrameric human GluN1/GluN2B receptor containing the extracellular and transmembrane parts [GluN1, UniProt (UniProt, 2021) Q05586, residues 23–861; GluN2B, UniProt Q13224, residues 30–852] was built using the previously created all-atom rat NMDAR model (Ladislav et al., 2018) with the automodel function of MODELLER version 9.23 (Webb and Sali, 2014). The rat model was based on the 4pe5, 4tll, and 4tlm template structures (C. H. Lee et al., 2014; Karakas and Furukawa, 2014). Side-chain positions in the human NMDAR model were further optimized, and the L825V mutations were introduced in both GluN2B subunits with FoldX version 5.0 (Schymkowitz et al., 2005).

Molecular dynamics (MD) simulations. The parameters of the implicit solvation/lipid membrane model (EEF1/IMM1; Lazaridis, 2003; J. Lee et al., 2016) were assigned using a web-based graphical

user interface CHARMM-GUI (Jo et al., 2008; J. Lee et al., 2016) following the protocol described earlier (Cerny et al., 2019). Langevin MD simulation of unliganded NMDAR spontaneous closing was then performed using the CHARMM version c41b1 MD package (Brooks et al., 2009). Pairs of GluN1/GluN2B and GluN1/GluN2B(L825V) simulations were started with identical initial random seed values. In each simulation, the geometry was collected every 10 ps over a 100 ns simulation time. Markov state modeling was performed using the PyEMMA module (Scherer et al., 2015) of the High-Throughput Molecular Dynamics package (Doerr et al., 2016). Markov states were assigned based on the all C_α root mean square deviation metric, and four states for the GluN1/GluN2B(L825V) and three states for the GluN1/GluN2B simulations were identified using a 0.1 ns lag time derived from the implied timescale plot. Representatives of each macrostate were stored as an ensemble of 20 randomly selected structures for further visualization in PyMOL (The PyMOL Molecular Graphics System, Version 2.4.0 Schrödinger, LLC) and VMD (Humphrey et al., 1996).

Mass spectrometry analysis
Hippocampus samples from 4-month-old males ($n = 4$ for +/+ and $n = 5$ for L825V/+) were lysed with several rounds of sonication in 100 mM triethylammonium bicarbonate, pH 7, containing 2% sodium deoxycholate (SDC). Cysteines were reduced and blocked. Protein concentration was determined using a bicinchoninic acid protein assay kit (Sigma-Aldrich), and 40 μg of protein per sample was digested with trypsin (Pierce) at 37°C overnight (Le et al., 2020). After digestion, SDC was removed by extraction to ethyl acetate (Masuda et al., 2008), and peptides were desalted using stage tips packed with C18 disks (Empore CDS) made in-house according to the manufacturer's protocol (Ishihama et al., 2006). Then, 16plex tandem mass tag (TMTpro) reagents were added to each sample, according to the manufacturer's protocol (Thermo Scientific Pierce). Labeled samples were pooled together, and 100 μg of labeled peptides were injected onto the C18 column (1.9 μm, C18, 300 × 0.3 mm; YMC) and separated by a linear gradient from 0% phase A (of 20 mM ammonium formate, 2% acetonitrile, pH 10) to 50% phase B (of 20 mM ammonium formate, 80% acetonitrile, pH 10), flowing at 3 μl/min for 60 min. Sixty-four fractions were collected and pooled into eight fractions (Kulak et al., 2017). The resulting fractions were dried and resuspended in 20 μl of 1% trifluoroacetic acid (Sigma-Aldrich).

Peptides were separated and analyzed on an UltiMate 3000 RSLCnano system coupled to an Orbitrap Fusion Tribrid mass spectrometer (both from Thermo Fisher Scientific). EASY-Spray column (75 μm × 50 cm; Thermo Fisher Scientific) was used for peptide separation in combination with trap column Acclaim PepMap300 (Thermo Fisher Scientific). A linear gradient from 5 to 35% of acetonitrile was used for separation for 180 min at a flow rate of 300 nl/min (McAlister et al., 2014).

Raw data were processed in Proteome Discoverer 2.5 (Thermo Fisher Scientific). TMT reporter ion ratios were used for the estimation of the relative amount of each protein. The search was done against *Mus musculus* and the common contaminant database. The modification was set: TMTpro label on peptide N terminus and lysine (unimod nr:2016), cysteine carbamidomethylation (unimod nr:39) as static, methionine oxidation (unimod nr:1384), and protein N-terminus acetylation (unimod nr:1) as variable. Proteins and peptides were filtered to 1% false discovery rate (FDR).

Data were normalized to total peptide amount, and all subsequent analyses were done in Perseus software (Tyanova and Cox, 2018). We filtered out contaminants and log transformed the intensities (binary logarithms). We filtered out proteins with insufficient number of valid quantification values, leaving only those with at least three values in at least one group. Student's *t* test with permutation-based FDR correction was used for the evaluation of significantly changed proteins at a 5% FDR level. ASD-related genes from the SFARI database (https://gene.sfari.org) were annotated.

Primary hippocampal cultures
Primary hippocampal microisland cultures were prepared as previously described (Smejkalova et al., 2021). Glass coverslips (24 mm; Glaswarenfabrik Karl Hecht) were coated with 0.15% agarose (Serva)

and let dry. Microdots (~200 μm in diameter, spaced ~200 μm apart) of a growth-permissive substrate containing 0.1 mg/ml poly-D-lysine (Sigma-Aldrich) and 0.2 mg/ml collagen (Serva) were stamped onto the coverslips. After decapitation, cortices and hippocampi were dissected from P0–1 mouse pups in HBSS (Invitrogen). Primary cortical astrocytes were prepared from +/+ mice, digested with trypsin (Invitrogen), mechanically dissociated, and cultured for 2 weeks in DMEM with GlutaMAX (Invitrogen), 10% FBS (Invitrogen/Invitrogen), and pen/strep (Sigma-Aldrich) at 37°C in 5% CO_2. Two days before hippocampal dissection, cultured astrocytes were trypsinized and plated on the microdot-stamped coverslips at a density of ~6,000 cells/cm². Newborn pups, the progeny of +/+ and L825V/+ crossings, were used to prepare primary hippocampal cultures without knowing the genotype. Hippocampi from each pup (P0–P1; female or male) were collected and treated separately from the tissue of other pups. A sample of the nervous tissue was taken and stored at −20°C for genotyping to be performed later. Hippocampi were digested in papain (Worthington Biochemical) at 37°C for 40 min and plated at a density of ~300 cells/cm² on top of the astrocyte microislands in a neuronal medium containing Neurobasal A with 2% B27 supplement (Invitrogen), GlutaMAX (Invitrogen), and pen/strep (Sigma-Aldrich). Microisland cultures were maintained at 37°C in 5% CO_2 until used for electrophysiological recordings.

Primary hippocampal mass cultures for immunofluorescence experiments were prepared from P0–P1 +/+ mouse hippocampus by triturating cells after partial trypsin digestion. Neurons were cultured on coverslips coated with 0.1 mg/ml poly-L-lysine (Sigma-Aldrich) in a Neurobasal medium containing 2% B27 supplement, L-glutamine (0.5 mM, Sigma-Aldrich), β-mercaptoethanol (25 μM, Sigma-Aldrich), and fibroblast growth factor basic FGF-b (10 ng/ml, Alomone Labs).

Electrophysiology
Recording from HEK293T cells. Electrophysiology experiments on cultured human embryonic kidney (HEK293T) cells transfected with cDNA encoding NMDAR subunits were performed 24–48 h after transfection. Whole-cell currents from HEK293T cells were recorded in the voltage-clamp mode using an Axopatch 200B amplifier (Molecular Devices), after the compensation of capacitance and series resistance (<10 MΩ) by 80–90%. Data were collected (sampled at 10 kHz and low-pass filtered at 2 kHz) and analyzed using a pClamp 10 software (RRID: SCR_011323, Molecular Devices). Electrophysiological experiments were performed at room temperature (RT; 21–25°C). Borosilicate glass pipettes (3–5 MΩ, Science Products) were filled with intracellular solution containing the following (in mM): 120 gluconic acid delta-lactone, 15 CsCl, 10 HEPES, 10 BAPTA, 1 $CaCl_2$, 3 $MgCl_2$, and 2 ATP Mg salt, pH adjusted to 7.2 with CsOH. Extracellular solution contained the following (in mM): 160 NaCl, 2.5 KCl, 10 glucose, 10 HEPES, 0.7 $CaCl_2$, and 0.2 EDTA, pH adjusted to 7.3 with NaOH. Glycine (10 μM), a coagonist of NMDARs, was present in all control and test solutions except when noted. All compounds were purchased from Sigma-Aldrich. Solutions were applied using a microprocessor-controlled multibarrel fast perfusion system. The solution exchange rate was estimated to be τ ~12.0 ms for dish-attached cells (Vyklicky et al., 2016). All recordings were performed at a holding potential of −60 mV and were not corrected for the liquid junction potential (−14 mV).

Recording from hippocampal neurons. Whole-cell patch-clamp recordings were acquired from hippocampal neurons [6–21 d in vitro (DIV)] held at −70 mV using a MultiClamp 700B amplifier (Molecular Devices). Data were sampled at 10 kHz and filtered at 2 kHz. Series resistance was 80% compensated. Recordings were discarded when the series resistance was >20 MΩ or increased by >20% during the recording. Patch electrodes (4–6 MΩ) from borosilicate glass capillaries contained the following intracellular solution (in mM): 125 potassium gluconate, 15 KCl, 10 HEPES, 5 EGTA, 0.5 $CaCl_2$, 2 ATP Mg salt, 0.3 GTP Na salt, and 10 creatine phosphate, pH adjusted to 7.2 with KOH. For agonist-evoked whole-cell responses, extracellular solution contained the following (in mM): 160 NaCl, 2.5 KCl, 10 HEPES, 10 glucose, 0.7 $CaCl_2$, 0.2 EDTA, and 0.010 glycine, pH adjusted to 7.3 with NaOH. Kainate (100 μM) or NMDA (100 μM) were used to evoke α-amino-3-hydroxy-5-methyl-4-isoxazolepropionic acid receptor (AMPAR) or NMDAR

currents, respectively, and tetrodotoxin (0.5 μM, Alomone Labs) was used to block action potentials.

Miniature excitatory postsynaptic currents (mEPSCs) were recorded in extracellular solution containing the following (in mM): 160 NaCl, 2.5 KCl, 10 glucose, 10 HEPES, 2 CaCl₂, and 1 MgCl₂, pH adjusted to 7.3 with NaOH. Evoked excitatory postsynaptic currents (eEPSCs) were elicited by a brief depolarization (1 ms at +10 mV) from the holding potential of −70 mV every 10 s in extracellular solution containing the following (in mM): 160 NaCl, 2.5 KCl, 10 glucose, 10 HEPES, 2 CaCl₂, and 0.010 glycine, pH adjusted to 7.3 with NaOH. To isolate NMDAR-EPSCs and AMPAR-EPSCs, 2,3-dioxo-6-nitro-1,2,3,4-tetra-hydrobenzo[f]quinoxaline-7-sulfonamide (NBQX; 3 μM, Tocris) and (2R)-amino-5-phosphonovaleric acid (AP-5; 50 μM, Tocris) were used, respectively. Ifenprodil (3 μM, Tocris) was used to inhibit responses mediated by NMDARs containing GluN2B subunits. All extracellular solutions contained bicuculline methochloride (10 μM, Tocris) to block γ-aminobutyric acid type A receptors (GABA_ARs). All compounds, unless otherwise stated, were purchased from Sigma-Aldrich. The amplitude and deactivation kinetics of eEPSCs were analyzed on the average of four consecutive eEPSCs. All measurements and analyses were performed blindly, with the genotype assigned later.

Channel P_o
The P_o was assessed from the kinetics of MK-801 (1 μM, Sigma-Aldrich) inhibition of responses to 1 mM glutamate fitted to the kinetic model using Gepasi (version 3.21). Glutamate binding steps were not considered because in the presence of 1 mM glutamate, NMDAR exists with a high probability [>99.6% as predicted from calculations using rate constants determined earlier (Cais et al., 2008)] in doubly liganded states with the channel closed (R) or open (O) and/or in a desensitized state (D):

$$D \underset{k_d}{\overset{k_r}{\rightleftharpoons}} R \underset{k_c}{\overset{k_o}{\rightleftharpoons}} O \underset{k_u}{\overset{k_b}{\rightleftharpoons}} B,$$
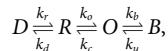
where B stands for the MK-801-blocked state. The fitting procedure consisted of two steps (Turecek et al., 2004). In the first step, the response induced by 1 mM glutamate in HEK293T cells transfected with WT or variant diheteromeric or triheteromeric receptors was analyzed for the peak (I_P) and steady-state response (I_{SS}), and the onset of desensitization was determined by a single-exponential function (τ_d). Desensitization (D) and the kinetic constants describing the onset of desensitization (k_d) and resensitization (k_r) were determined from Equations 1–3:

$$D = 1 - (I_{SS}/I_P), \quad (1)$$

$$k_d = D/\tau_d, \quad (2)$$

$$k_r = (1 - D)/\tau_d. \quad (3)$$

In the second step, k_d and k_r were fixed at values obtained from the first step, and the rate of closing (k_c) was set to an arbitrary value of 200 s⁻¹. The NMDAR response recorded in the presence of 1 mM glutamate and 1 μM MK-801 was fitted to the model, while the opening rate (k_o) was set as a free parameter. MK-801 blocking rate (k_b) was set to 25 μM⁻¹ s⁻¹ (Huettner and Bean, 1988; Jahr, 1992; Rosenmund et al., 1995). Macroscopic P_o was calculated as follows:

$$P_o = 100 \times k_o/(k_o + k_c). \quad (4)$$

DNA constructs
The human GluN2B (hGluN2B; GenBank accession no. NP_000825) subunit in the expression vector pCI-neo was a generous gift from Prof. Traynelis. To analyze the functional consequences of the GluN2B(L825V) variant, we used human GluN1-1a (hGluN1-1a; GenBank accession no. NP_015566; a gift from Prof. Traynelis), rat GluN1-1a (rGluN1-1a; GenBank accession no. U08261), rat GluN2A (rGluN2A; GenBank accession no. D13211), and rat GluN2B (rGluN2B; GenBank accession no. M91562) expressed in HEK293T cells.

The L825V variant in hGluN2B and rGluN2B was introduced by QuikChange site-directed mutagenesis kit (Agilent). To selectively express triheteromeric NMDARs at the cell surface, we used two different C-terminal peptide tags as previously described (Hansen et al., 2014). The rGluN2B subunit coupled through a short polypeptide linker to one of two different leucine zipper motifs followed by endoplasmic reticulum (ER) retention motifs (C1 and C2 variants) from γ-aminobutyric acid type B receptors (GABA_BRs; a generous gift from Prof. Traynelis) was replaced with the hGluN2B subunit employing the in vivo assembly (IVA) cloning method (Garcia-Nafria et al., 2016). Subsequently, the L825V variant was introduced to the hGluN2B-C1 and hGluN2B-C2 constructs by IVA cloning. Due to the different lengths of C-terminal domains (CTDs) in rGluN2A and rGluN2B subunits (626 and 644 amino acids, respectively), to express triheteromeric rGluN1-1a/rGluN2A/rGluN2B receptors, the rGluN2B subunit containing the rGluN2A CTD was used. We used this approach to ensure that the leucine zipper motifs in the C1 and C2 tags can interact appropriately to mask the ER retention signals and allow the receptor to be expressed at the cell surface. For the analysis of receptor localization, eGFP tag was introduced into hGluN2B subunits directly after the signal peptide in the extracellular portion of the receptor using IVA cloning. Subsequently the eGFP-tagged hGluN2B subunit was transferred by classical restriction enzyme cloning into pLEX-MCS (Thermo Fisher Scientific) expression vector for lentiviral transduction. The sequences of all constructs were confirmed by Sanger sequencing (Eurofins).

Analysis of surface expression and synaptic localization by fluorescence microscopy
Methods for the analysis of cell surface expression of NMDAR subunits have been described in detail (Kuchtiak et al., 2024). Lentiviral particles were produced in HEK293T cells transfected using a GenJet transfection reagent (SignaGen Laboratories) with the following constructs: pLEX-MCS containing the gene encoding the eGFP-hGluN2B subunit, packaging plasmid (pCMVΔ8.1), and envelope plasmid (pMD.VSVG), at a ratio of 3.5:2.5:1. Twenty-four hours after transfection, media were collected for the first time, stored at 4°C, and replaced by fresh media. Seventy-two hours after transfection, media were collected for the second time. The collected media were filtered through a cellulose acetate membrane filter (0.45 μm pore size, Ahlstrom-Munksjö). Lentiviruses were concentrated by ultracentrifugation of media at 50,000g for 2.5 h. Primary hippocampal mass cultures prepared from newborn +/+ mice were treated with lentivirus containing the construct encoding the eGFP-tagged hGluN2B (WT or L825V) subunit at 4 DIV. At 14 DIV cells were washed with phosphate-buffered saline (PBS), fixed with 4% para-formaldehyde (PFA)/4% sucrose (in PBS) for 10 min and blocked for 30 min with PBS containing 50 mM NH₄Cl, 10% goat serum, and 2% fish gelatin (all from Sigma-Aldrich). To determine surface receptor expression, cells were initially incubated with a primary anti-GFP antibody (1:500; rabbit, AB3080P; Roche) for 45 min at RT, washed, and further incubated with a secondary antibody Alexa Fluor 647 (1:500; goat anti-rabbit, A-21244; Invitrogen), again for 45 min at RT. To assess intracellular receptor expression, cells were washed and permeabilized using a permeabilization blocking solution additionally containing 0.1% Triton X-100 (Carl Roth) and 0.1% Tween 20 (Sigma-Aldrich) for 30 min. Intracellular receptors were stained by incubating the cells with the same primary antibody for 1 h at RT and subsequently with an Alexa Fluor 488 secondary antibody (1:500; goat anti-rabbit; A-11034; Invitrogen), again for 1 h at RT. Additionally, together with the staining of intracellular receptors, we labeled synapses with an anti-PSD-95 antibody (1:500; mouse, K28/43; NeuroMab) followed by a secondary antibody Alexa Fluor 555 (1:500; goat anti-mouse; A-21422; Invitrogen). Cell nuclei were visualized using the DAPI fluorescent dye (1:2,000; D1306; Invitrogen). Finally, cells were mounted with a ProLong Glass mounting medium (Invitrogen). Images were obtained on a Leica DMi8S microscope equipped with a sCMOS camera (Leica DFC9000 GTC) and captured as z-stack images (z-step size, 0.18 μm) with PlanAPO 63× (1.47 NA) oil-immersion objective (Leica) at 395 nm (DAPI), 488 nm (hGluN2B intracellular), 555 nm (PSD-95), and 647 nm (hGluN2B cell surface) excitation wavelengths.

To verify that the native fluorescence intensity of eGFP was negligible compared with the intensity of Alexa Fluor 488, we compared the fluorescence intensity of HEK293T cells transfected with eGFP-hGluN2A WT and hGluN1-1a [using a GenJet transfection reagent (SignaGen) according to the manufacturer's protocol] that were either fixed and permeabilized as described above but not immunostained, or fixed and permeabilized and immunostained [PBS containing 50 mM NH_4Cl, 10% goat serum, 2% fish gelatin, 0.1% Triton X-100, and 0.1% Tween 20 with an anti-GFP primary antibody (1:1,000; rabbit, AB3080P; Roche)] followed by an Alexa Fluor 488 secondary antibody (1:1,000; goat anti-rabbit; A-11034; Invitrogen), each incubated with cells at RT for 45 min. Images were captured at the excitation wavelength of 488 nm as described above. The images were analyzed using ImageJ as a maximum projection of the z-stacks, where the average intensity in channel 488 (subtracted from the intensity of the background) was measured. We found that native eGFP fluorescence intensity was $6 \pm 1\%$ ($n = 70$ transfected cells from two cultures) of the fluorescence intensity of Alexa Fluor 488 ($n = 87$ transfected and immunostained cells from two cultures).

Dead neurons were excluded based on the DAPI staining. The imaging parameters were set to avoid saturation of pixel intensities and were kept constant throughout the imaging for each experiment. Images were acquired in 16-bit format with a pixel size of 103 nm. The images were then deconvolved by the Huygens software version 21.04 (Scientific Volume Imaging) using the classic maximum likelihood estimation algorithm and further analyzed using the ImageJ software version 1.53t (NIH): (1) Surface expression was analyzed from the maximum z-stack projections, where the average intensities in channels 488 and 647 (after subtracting the intensity of the background) in the soma and dendritic spines were measured [from each neuron, five dendritic spines were selected from five different segments of dendrites (secondary or higher) using the PSD-95 signal]. Surface expression was determined as the ratio of these intensities, i.e., surface and intracellular labeling, and data obtained from the different spines originating from the same neuron were averaged. The values of surface/intracellular fluorescence ratio were then normalized to the mean ratio values for eGFP-hGluN2B WT. (2) Mander's overlap coefficient determining the degree of colocalization between surface eGFP-hGluN2B and a synaptic marker PSD-95 was calculated from one 20 μm segment of secondary dendrite per neuron using the ImageJ plugin Coloc2 with automatic bisection thresholding. (3) The percentage of surface eGFP-hGluN2B labeling overlapping with PSD-95 (indicating synaptic localization) was also calculated from the same dendritic segments as described above using our own macro, where after the maximum z-stack projection, adaptive thresholding was performed (ImageJ plugin). Masks of surface eGFP-hGluN2B and PSD-95 labeling were created, the PSD-95 mask was subtracted from the surface eGFP-hGluN2B mask, and the percentage of surface eGFP-hGluN2B pixels overlapping with PSD-95 was calculated.

Analysis of synaptic localization by super-resolution STED microscopy
Neurons from +/+ mice were prepared and transduced as described above. At 14 DIV cells were washed with PBS, fixed with PFA, and blocked for 30 min with PBS containing 50 mM NH_4Cl, 10% donkey serum, and 2% fish gelatine. To label eGFP-tagged hGluN2B subunits, cells were initially incubated with a nanobody Fluotag-anti-GFP-STAR635P (1:100; N0301, NanoTag Biotechnologies) for 1 h. Cells were further washed and permeabilized using a permeabilization blocking solution additionally containing 0.1% Triton X-100 and 0.1% Tween 20 for 30 min. Synapses were labeled by incubation with an anti-PSD-95 antibody (1:500; mouse, K28/43; NeuroMab) followed by a secondary antibody STAR580P (1:100; goat anti-mouse; Abberior Instruments), each for 1 h. Finally, the cells were mounted with a ProLong Glass mounting medium. Images were obtained on the Abberior Instruments Expert Line STED system (Abberior Instruments) equipped with a Nikon Eclipse Ti-E microscope body and a Nikon CFI Plan Apo Lambda 60× oil, NA 1.40 objective. The sample was illuminated with pulsed 561 and 640 nm lasers and depleted by a pulsed 775 nm STED depletion laser of a 2D donut shape formed by a spatial light modulator. The fluorescence signal was filtered (emission bandpasses, 580–630 and 650–720 nm; pinhole, 50 μm) and detected on single-photon counting modules (Excelitas

Technologies), with time gates set to 0.75–8 ns. Images were scanned with a pixel size of 25×25 nm, with a 10 μs dwell time and in-line interleaved acquisition mode using the Imspector software (Abberior Instruments). Confocal images were acquired using the 561 and 640 nm lasers in the conventional confocal mode. The STED images were then deconvolved by the Huygens software using the classic maximum likelihood estimation algorithm and further analyzed using the ImageJ software: (1) Mander's overlap coefficient determining the degree of colocalization between surface eGFP-hGluN2B and PSD-95 was calculated in the STED-deconvolved images for regions of interest (ROIs) of dendritic spines (one dendritic spine ROI per neuron was selected from the confocal images of the PSD-95 staining) using the ImageJ plugin Coloc2 with automatic bisection thresholding. (2) The percentage of surface eGFP-hGluN2B labeling overlapping with PSD-95 (indicating synaptic localization) was also calculated from the same dendritic spine ROIs as described above using our own macro, where the Huang segmentation algorithm was performed. Masks of surface eGFP-hGluN2B and PSD-95 labeling were created, the PSD-95 mask was subtracted from the surface eGFP-hGluN2B mask, and the percentage of overlapping pixels was calculated.

Behavioral analysis
Behavioral testing was carried out during the light phase of the cycle using L825V/+ animals and their +/+ littermates. All work with animals was performed with the approval of the Czech Central Commission for Animal Welfare in accordance with institutional and national guidelines. Animals were tested at 9–15 weeks of age. Males and females were tested separately on different days. Animal enclosures or testing mazes were carefully cleaned with 75% alcohol solution and then dried to remove olfactory traces before the first and between individual animals tested. The analyses were performed in the following order: open-field test, prepulse inhibition (PPI) test, and contextual and cued fear conditioning. A separate cohort of animals was used for testing in the IntelliCage system.

Open-field test. A cubic box without a top with the dimensions of 42×42 cm uniformly illuminated with the light intensity of 200 lux was used as previously described (Kulesskaya and Voikar, 2014). The area was virtually divided into periphery and center zone, where the center zone constituted 38% of the whole arena. Each mouse was initially placed in the corner of the area and given a 10 min period of free maze exploration. Time spent in each zone, distance traveled, average speed, and other derived parameters were automatically computed based on a video tracking system (Viewer, Biobserve).

PPI test. Testing was performed in soundproof cabinets and the execution protocol was controlled by software (Med Associates). The test was initiated following habituation to the holder for 10 min. Four prepulse acoustic stimuli (70, 77, 82, 85 dB; 20 ms) were used for prepulse alone or with a startle stimulus (110 dB; 50 ms). White noise was used for stimuli, and all recording and stimulus delivery was made with a constant background noise of 65 dB. The prepulse/startle stimulus delay was 120 ms. Ten repetitions of startle, prepulse, and a combination of prepulse with startle were conducted in random order. Intertrial interval varied randomly between 10 and 20 s. The PPI value is presented as the percentage of the startle response decrease ($100 * (SR - PreSR) / SR$), where SR is the response to the startle stimulus and PreSR is the response to the combined prepulse with the startle stimulus. All animal reactions to the delivered stimuli were detected and amplified, and their quantified amplitude was graphically represented and stored automatically by the sensor platform, amplifier, and the computer software, respectively.

Cued and contextual conditioning test. Testing took place in a conditioning cage in a soundproof cabinet (Ugo Basile). The cage was equipped with a stainless steel rod floor for shock delivery. The acquisition trial started with an adaptation period lasting 4 min, after which mice were presented with two pairings of the conditioned stimulus (20 s of 4 kHz pure tone at 77 dB) and the unconditioned stimulus (1 s, 0.5 mA constant current to the cage floor; Stiedl et al., 1999). The unconditioned stimulus was presented with the termination of the conditioned stimulus, and the interval between the two pairings was 2 min. Mice were tested for contextual memory 24 h after learning in

the same context. The dependent measure was freezing, recorded automatically by the ANY-maze software (Ugo Basile) during a 6-min-long trial. For delayed cued memory testing, mice were introduced to a novel context with different wall patterns, smooth floor texture, and vanilla scent 3 h after the contextual trial. The freezing response to a 2-min-long conditioned stimulus was monitored.

Behavioral assessment in the IntelliCages. Mice were housed for 38 d in the IntelliCage system (TSE Systems), an apparatus for automatic, long-term, high-throughput monitoring of cognitive abilities and emotional state in group-housed laboratory mice. A week before being moved to the IntelliCage, all animals were injected with subcutaneous transponders (ISO-compliant transponders). Four experimental groups, two mixed-genotype groups of males (10 animals per cage) and two mixed-genotype groups of females (nine animals per cage), were tested in separate cages (38 animals in total). The IntelliCages were equipped with four operant corners, each with two door-guarded openings to drinking bottles. Each corner also had a radio-frequency identification antenna detecting implanted transponders and allowing the identification of an animal entering the corner. The selected corner rewards the animal by providing access to water upon a correct nosepoke on the door (Kiryk et al., 2020). Animals were tested in several phases. During the initial free adaptation phase lasting 4 consecutive days, all corners had doors open and mice had free access to water. During the subsequent nosepoke adaptation phase lasting 4 consecutive days, all doors were initially closed, and the first nosepoke opened the door for 5 s. The animals had to leave the corner and start a new visit to drink more. The nosepoke adaptation phase is the initial phase for the subsequent five consecutive phases with restricted water access: (1) During the drinking phase, the animals had access to water restricted to two 2-h-long sessions, the first at 21:00–23:00 and the second at 3:00–5:00. Water availability was guided by constant blue LED lighting in each corner. Upon each nosepoke, the door opened for 7 s, once per visit. This phase lasted 4 d. (2) The place preference phase differed from the previous by limiting water access to only one corner randomly assigned to each animal and balanced among all four corners. This phase lasted 5 d. (3) In the place preference reversal phase, the rewarded corner was changed to the one diagonally opposite for the next 5 d. (4) Next, in the preference decline phase, mice were put back on the drinking phase protocol for 7 d (Benner et al., 2014). (5) Finally, in the clockwise patrolling phase, the rewarded corner was changed to the following one in the clockwise order only when the mouse had made a correct response (nosepoke in the correct corner). This phase lasted 5 d (Kobayashi et al., 2013; Benner et al., 2014).

Statistical analysis
Data are presented in bar graphs showing mean ± standard error of the mean (SEM), or in scatter plots showing the distribution of individual cells overlaid on bar graphs showing mean ± SEM. Sample size n refers to the number of cells or animals (independent values) per group. Statistical analysis was performed with STATGRAPHICS Centurion 18 (Statgraphics Technologies). If the original data did not have a symmetric distribution and constant variance, they were power transformed to attain symmetric distribution and homoscedasticity (constant variance). We used absolute values of studentized residuals >3 to identify outliers. Data were further analyzed by the analysis of variance (ANOVA), using the general linear model function in STATGRAPHICS. When the results showed statistically significant differences, the analysis was followed by post hoc comparisons using the Duncan method or the least significant difference method. $P \leq 0.05$ was considered statistically significant throughout the study. In the case of experiments where data were collected with respect to cell age in vitro, we divided the days (DIV) into four age groups with approximately the same number of data points in each group, to be able to see the trend with respect to age. Afterward, we analyzed these groups using ANOVA (using the general linear model function in STATGRAPHICS).

Results

GluN2B(L825V) subunit reduces NMDAR P_o
Based on our previous results characterizing the functional consequences of disease-associated variants located in the membrane

domain of the NMDAR (Vyklicky et al., 2018), we selected the variant GluN2B(L825V) to explore its effects in more detail. The de novo missense variant (c.2473T>G; p.L825V) in the *GRIN2B* gene had been identified in a male patient with ID and ASD with no immediate family history of neuropsychiatric disorders (Fig. 1A; Awadalla et al., 2010; Tarabeux et al., 2011). This patient, evaluated at 7 years of age, had no history of encephalitis, epilepsy, Tourette's syndrome, or other diseases. His EEG and CT scan results were normal. He did not speak, eat on his own, or play with/handle objects with his hands (Dr. Guy Rouleau, McGill University, personal communication).

Recombinant human GluN1/GluN2B(L825V) receptors are characterized by a dramatic reduction of P_o (Vyklicky et al., 2018), which underlies a loss-of-function phenotype at the receptor level. In the heterozygous condition, at early developmental stages, when GluN2B is dominantly expressed (Sheng et al., 1994), it is expected that in addition to WT diheteromeric GluN1/GluN2B receptors, variant diheteromeric (GluN1/GluN2B(L825V)) and triheteromeric (GluN1/GluN2B/GluN2B(L825V)) receptors may occur. Later in development, when GluN2A is also expressed, additional subunit combinations may arise—triheteromeric GluN1/GluN2A/GluN2B (Luo et al., 1997; Rauner and Kohr, 2011; Tovar et al., 2013; Hansen et al., 2014) and GluN1/GluN2A/GluN2B(L825V). Thus, we analyzed the functional consequences of the GluN2B(L825V) variant in triheteromeric receptors containing one WT GluN2A or GluN2B subunit (Fig. 1). We employed receptor subunits with C1 or C2 tags introduced at the end of the GluN2 CTDs (Hansen et al., 2014). These tags consist of modified leucine zipper motifs followed by ER retention motifs from GABA$_B$Rs. The C1/C2 tag combination is required for the formation of a coiled-coil structure masking the ER retention signals, resulting in the preferential cell surface expression of triheteromeric receptors, e.g., containing variant GluN2B(L825V) together with WT GluN2A or GluN2B (Fig. 1B), while the diheteromeric C1/C1 and C2/C2 combinations remain in the ER. The modified NMDAR subunits were coexpressed in HEK293T cells and activated by a saturating concentration of glutamate (1 mM). Subsequently, the open-channel blocker MK-801 (1 μM) was applied, and the rate of the MK-801 inhibition was fitted to the kinetic model to determine the P_o (see Materials and Methods and Eqs. 1–4). The P_o of hGluN1/hGluN2B-C1/hGluN2B-C2 receptors was determined to be 9.9 ± 1.0% ($n = 6$; Fig. 1D). This value is not significantly different from that determined in hGluN1/hGluN2B receptors without the C1 and C2 tags ($P_o = 7.6 \pm 0.9\%$; $n = 9$; $p = 0.055$, Duncan method). These values are similar to those determined for rGluN1/rGluN2B receptors by various approaches earlier (N. Chen et al., 1999; Korinek et al., 2015; Ladislav et al., 2018; Vyklicky et al., 2018).

Superimposed traces in Figure 1C indicate that in hGluN1/hGluN2B-C1/hGluN2B(L825V)-C2 receptors, the onset of MK-801 inhibition was decelerated compared with hGluN1/hGluN2B-C1/hGluN2B-C2 receptors. The analysis indicated that in variant triheteromeric hGluN1/hGluN2B-C1/hGluN2B(L825V)-C2 receptors, the P_o was significantly decreased ($P_o = 4.9 \pm 0.8\%$; $n = 7$; $p < 0.001$, Duncan method) to values that were intermediate between WT diheteromeric hGluN1/hGluN2B-C1/hGluN2B-C2 and variant diheteromeric hGluN1/hGluN2B(L825V)-C1/hGluN2B(L825V)-C2 receptors ($P_o = 1.0 \pm 0.1\%$; $n = 5$). Similarly, in triheteromeric rGluN1/rGluN2A-C1/rGluN2B(L825V)-C2 receptors, the P_o (23.4 ± 3.1%; $n = 6$) was significantly decreased compared with triheteromeric rGluN1/rGluN2A-C1/rGluN2B-C2 receptors ($P_o = 34.6 \pm 3.4\%$; $n = 6$; $p < 0.001$, Duncan method; Fig. 1D). Thus, we show that the presence of a single
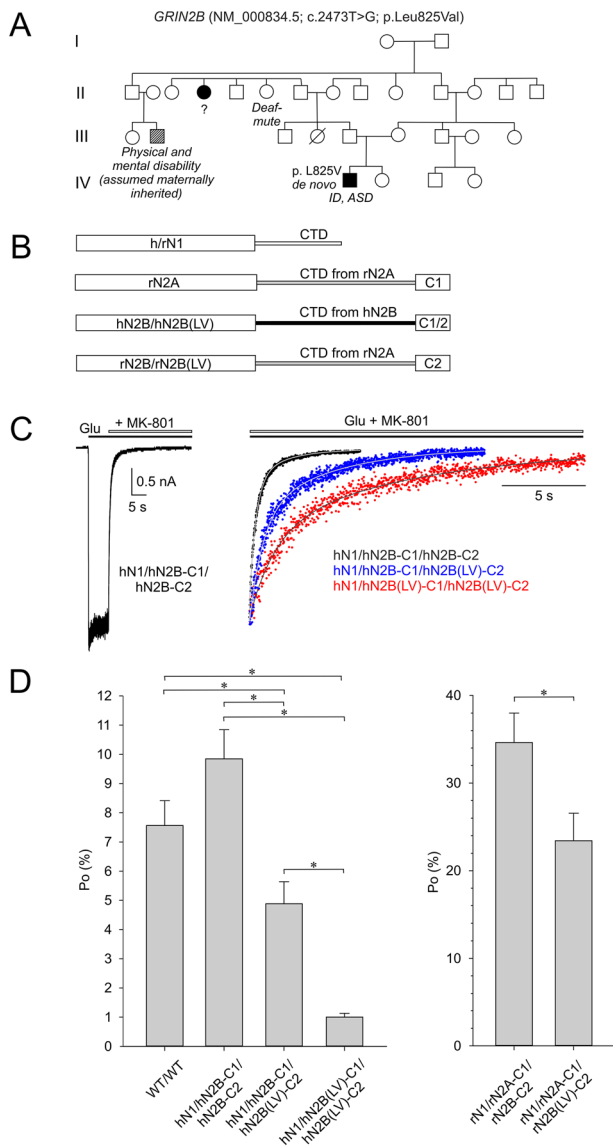
Figure 1. ID-/ASD-associated variant GluN2B(L825V) reduces P_o in diheteromeric and triheteromeric NMDARs. ***A***, Pedigree of the proband diagnosed with ID/ASD and identified to be a carrier of a de novo likely pathogenic mutation in *GRIN2B* (NM_000834.5; c.2473T>G; p.Leu825Val). ***B***, Linear representations of the subunit polypeptide chains showing the CTD of GluN1 (white), the CTD of GluN2A (gray) tagged with C1, the CTD of GluN2B (black) tagged with C1 or C2, and a chimeric GluN2B subunit with its CTD replaced by the GluN2A CTD tagged with C2 [*h* and *r* stand for the human and the rat isoform, N1 for GluN1, N2A for GluN2A, N2B for GluN2B, and N2B(LV) for GluN2B(L825V)]. ***C***, Left, typical response of hGluN1/hGluN2B-C1/hGluN2B-C2 receptors to the application of 1 mM glutamate in the continuous presence of 10 μM glycine, followed by the addition of 1 μM MK-801. Right, normalized current responses (indicated as dots) show the onset of MK-801 inhibition of responses to glutamate. The time course of the onset of MK-801 inhibition was best described by $P_o = 10.9\%$ for hGluN1/hGluN2B-C1/hGluN2B-C2 (hN1/hN2B-C1/hN2B-C2) receptors (gray line), $P_o = 4.8\%$ for hGluN1/hGluN2B-C1/hGluN2B(L285V)-C2 (hN1/hN2B-C1/hN2B(LV)-C2) receptors (blue line), and $P_o = 0.9\%$ for hGluN1/hGluN2B(L825V)-C1/hGluN2B(L825V)-C2 (hN1/hN2B(LV)-C1/hN2B(LV)-C2) receptors (red line; see Materials and Methods for the details of the analysis procedure). ***D***, Graphs show mean $P_o \pm$ SEM for hGluN1/hGluN2B without the C1 or C2 tags (WT/WT) and diheteromeric and triheteromeric NMDARs as indicated. * Marks significant differences. Data were power transformed and tested using ANOVA followed by pairwise comparisons using the Duncan method.

GluN2B(L825V) subunit leads to the reduction of the P_o of NMDARs containing either GluN2A or GluN2B in addition.

Since some hGluN2B-C1/hGluN2B-C1 and hGluN2B(L825V)-C2/hGluN2B(L825V)-C2 receptors may have escaped ER retention

and could also contribute to the measured current, we performed control experiments following the protocol previously used by Hansen et al. (2014). We generated hGluN2B(R519K + T691I)-C1 subunit with mutations in the agonist-binding pocket that abolish glutamate binding (Laube et al., 1997; Hatton and Paoletti, 2005; Erreger et al., 2007). Glutamate responses induced in HEK293T cells transfected by hGluN1, hGluN2B(R519K + T691I)-C1, and hGluN2B-C2 can arise only from escaped diheteromeric hGluN1/hGluN2B-C2 receptors. The responses induced in HEK293T cells transfected with hGluN1, hGluN2B(R519K + T691I)-C1, and hGluN2B-C2 subunits were -0.83 ± 0.35 pA/pF ($n = 5$), while the control responses induced in cells transfected with hGluN1, hGluN2B-C1, and hGluN2B-C2 were -11.7 ± 3.6 pA/pF ($n = 7$). These results indicate that the "escape" current was only ~7% of control and should have a negligible effect on the results obtained.

Molecular modeling of the effects of the GluN2B(L825V) variant

We used MD simulations to explore possible effects of the GluN2B(L825V) variant on receptor transitions between closed and open states. We based our approach on the previously described analysis of a homology model of the rat GluN1/GluN2B receptor (Cerny et al., 2019). MD simulations of spontaneous closing of the unliganded homology model of the human GluN1/GluN2B receptor (Fig. 2A,B) suggest a closing mechanism qualitatively identical to that we have described for rat GluN1/GluN2B (Cerny et al., 2019). In response to the missing glycine and glutamate ligands, the extracellular domains (N-terminal domain and ABD) rotate significantly with respect to the membrane-anchored TMD, and the receptor reaches the closed state with a nonsymmetrical orientation of the M3 helices through an iris-like transition typically within tens of nanoseconds of simulation time. The Markov state analysis of the human GluN1/GluN2B closing trajectory identified a highly populated (89%) state corresponding to the fully closed state of the receptor. Visualization of representative structures from this state shows a compact ensemble with relatively low diversity in the TMD. The structure ensemble and the distribution of the gating Thr C_α positions are summarized in Figure 2C–E. When the receptor is closing, the GluN2B ABDs are no longer pulling the connected M3 helices apart, and their across-the-channel distance decreases. The tightly interacting GluN2B M3 helices are responsible for the primary gating at the level of the TTTT (GluN2B T647 and GluN1 T648) residues.

The human diheteromeric GluN1/GluN2B(L825V) receptor shows a significantly different behavior (Fig. 2F–H). The Markov state analysis of the L825V closing trajectory identified two fully closed states with similar energies, populations, and geometries, representing over 85% of the simulation data. The ensemble of representative closed structures reveals a higher overall mobility of the TMD M3 helices as well as of the outer wall of the M1 and M4 helices. Especially the GluN1 M3 helices, facing the smaller GluN2B M4 L825V residue, are more separated (by ~2 Å on average) than in the closed state of the WT GluN1/GluN2B receptor. The GluN1 M3 helices also form tighter contacts with the GluN2B M1 and M4 helices. Surprisingly, although the GluN1 M3 helices are more separated, the L825V closed structures involve a tight across-the-channel interaction of GluN1 L657 residues belonging to the auxiliary LILI gate (GluN2B I655 and GluN1 L657) that plays a role in transducing the pulling motion between the ABD and the M3 helices (Ladislav et al., 2018). As a result of this interaction, channel opening may be less efficient in the L825V receptor, underlying the reduced P_o.
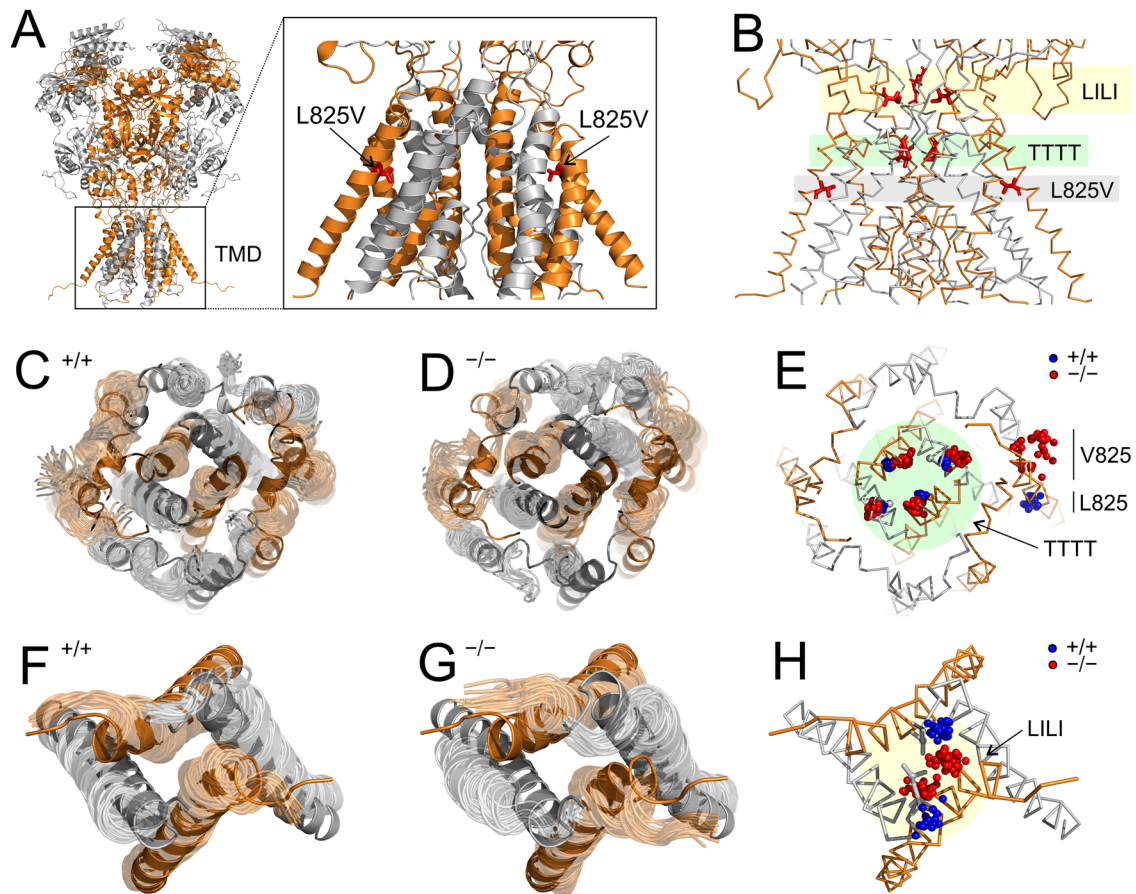
Figure 2. Summary of the L825V variant effects on the closed-state geometry of the NMDAR. **A**, The domain architecture of the GluN1(gray)/GluN2B(orange) receptor is shown in a crystal structure derived from the homology model with the L825V position in the TMD highlighted by red sticks. **B**, A schematic depiction of the positions of selected residues in the TMD. From the top are shown the auxiliary gating LILI (GluN2B I655 and GluN1 L657) residues with yellow background, the channel gating TTTT (GluN2B T647 and GluN1 T648) residues with green background, and the L825V positions with gray background. **C**, Top view at the TTTT level of the TMD showing an ensemble of MD snapshots representing closed-state structures of the human WT NMDAR (transparent) superimposed onto the initial crystal-like homology model (opaque). **D**, Top view at the TTTT level of the TMD showing an ensemble of MD snapshots representing closed-state structures of the human L825V NMDAR (transparent) superimposed onto the initial crystal-like homology model (opaque). **E**, Comparison of positions and mobility of the TTTT and L825/V825 residues summarizing data from panels **C** and **D**. The Cα atoms in the WT and variant receptor are shown as blue and red spheres, respectively. **F**, Top view at the LILI level of the TMD showing an ensemble of MD snapshots representing closed-state structures of the human WT NMDAR (transparent) superimposed onto the initial crystal-like homology model (opaque). **G**, Top view at the LILI level of the TMD showing an ensemble of MD snapshots representing closed-state structures of the human L825V NMDAR (transparent) superimposed onto the initial crystal-like homology model (opaque). **H**, Comparison of positions and mobility of the GluN1 L657 residues summarizing data from panels **F** and **G**. The Cα atoms in the WT and variant receptor are shown as blue and red spheres, respectively.

Reduced NMDA-induced whole-cell current in hippocampal cultures from L825V/+ mice

To evaluate the effect of the GluN2B(L825V) variant in the native context, we used CRISPR/Cas9 gene editing to introduce the corresponding variant to the mouse *Grin2b* gene (Fig. 3A). NMDAR currents were examined in primary hippocampal microisland cultures prepared from newborn heterozygous L825V/+ and WT +/+ mice and cultured for 6–21 DIV. The expression of GluN2 subunits is developmentally regulated, and the developmental pattern is also preserved in cultured neurons. Using standard whole-cell voltage-clamp techniques in excitatory neurons, we measured whole-cell responses induced by the application of 100 μM kainate or 100 μM NMDA (in the presence of 10 μM glycine) at a holding potential of −70 mV. The peak of the agonist-induced current was normalized to the whole-cell capacitance to exclude the effect of neuronal cell size. As shown in Figure 3B, the current density of AMPA/kainate receptor (AMPAR) responses to kainate was not different between +/+ and L825V/+ neurons, increasing with the age of culture for both genotypes (ANOVA: $p = 0.99$ for genotype, $p < 0.001$ for

age). In contrast, the analysis of NMDAR current densities indicates that in L825V/+ neurons the densities were on average smaller than in +/+ neurons, with an increase in NMDAR current densities in both genotypes as a function of development (Fig. 3C; ANOVA: $p < 0.001$ for both genotype and age).

Next, we used ifenprodil, a selective inhibitor of NMDARs containing the GluN2B subunit (Williams, 1993), to explore the source of the reduced NMDAR current densities in L825V/+ neurons (Fig. 3D). Control experiments were performed to exclude the possibility that the ifenprodil inhibitory effect might be affected by the variant GluN2B subunit. At a concentration of 0.15 μM, ifenprodil inhibited recombinant GluN1/GluN2B receptors by $62.0 \pm 3.3\%$ ($n = 7$) and GluN1/GluN2B(L825V) receptors by $63.1 \pm 4.3\%$ ($n = 6$; $p = 0.836$). The degree of ifenprodil (3 μM) inhibition of NMDA-induced currents in hippocampal neurons decreased with the age of the culture, consistent with the developmental switch between GluN2B and GluN2A subunits in both genotypes (ANOVA: $p < 0.001$ for age). Since NMDARs containing the GluN2B(L825V) subunit have a low P_o, it would be expected that in the absence of any other effect,
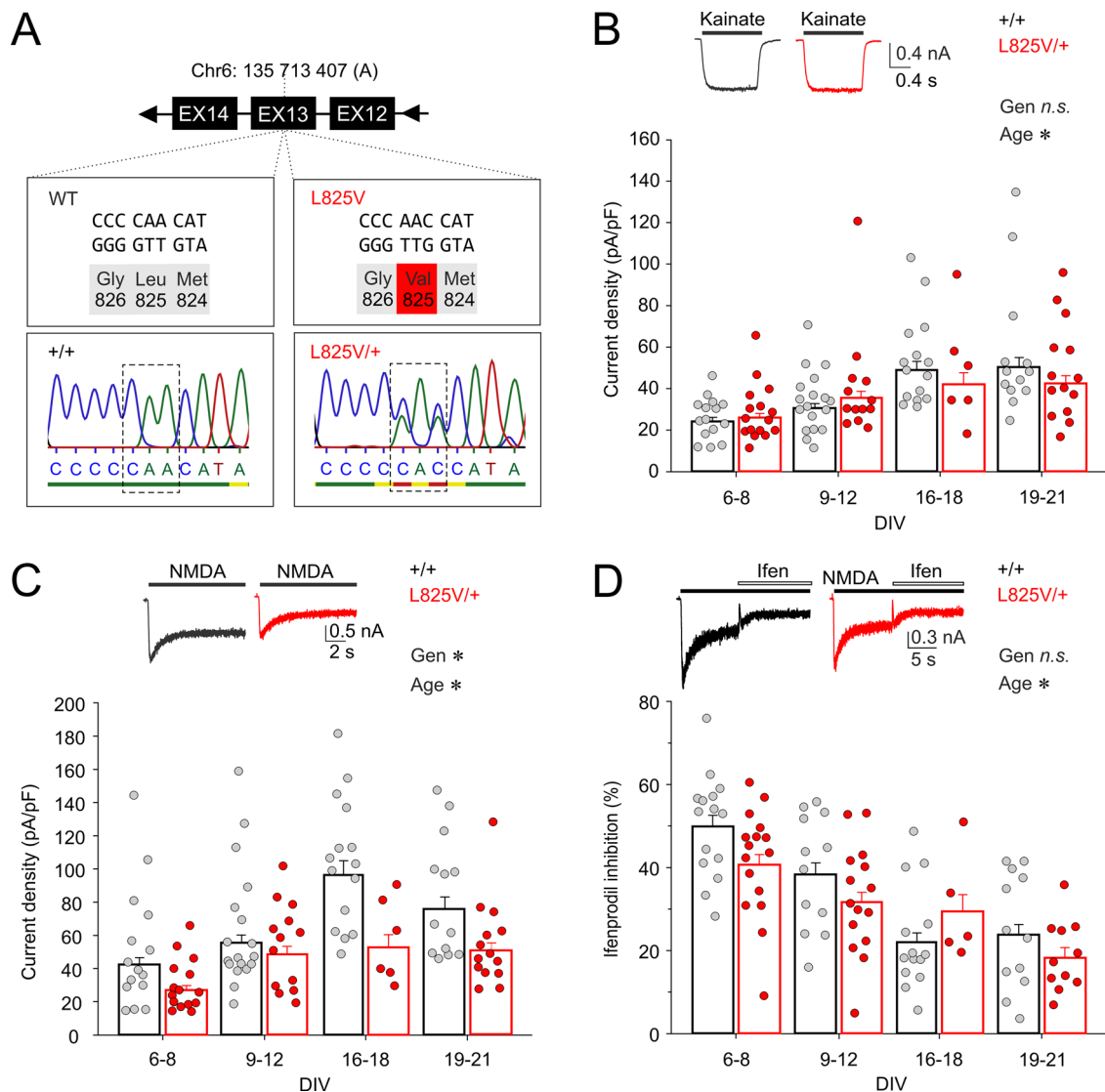
Figure 3. NMDAR but not AMPAR whole-cell currents are reduced in L825V/+ neurons. **A**, The position of the L825V variant within the mouse chromosome (chr6: 135 713 405–407) according to the GRCm39/mm39 assembly. Two bases T to G and G to T in the codon for leucine (TTG) were edited to create the new codon for valine (GTT). Two chromatograms show the results of Sanger sequencing of PCR amplicons of genomic DNA from +/+ and L825V/+ individuals containing the region of the L825V variant. **B**, **C**, Scatter plots show the current density distribution in individual hippocampal neurons by age in vitro; bar graphs show mean ± SEM for each genotype and age group. Currents were induced by 100 µM kainate (**B**) or 100 µM NMDA in the presence of 10 µM glycine (**C**). Insets show representative whole-cell responses evoked by kainate or NMDA in neurons prepared from +/+ (black) or L825V/+ (red) animals and cultured for 21 DIV. **D**, The scatter plot shows the distribution of ifenprodil (3 µM) inhibition of NMDA-evoked currents recorded in individual neurons by age in vitro; the bar graph shows mean ± SEM for each genotype and age group. Inset shows the effect of 3 µM ifenprodil on responses to 100 µM NMDA in neurons prepared from +/+ (black) or L825V/+ (red) animals cultured for 21 DIV. Data (obtained from n = 5–18 neurons from 3 to 7 animals per group) were power transformed and tested using ANOVA. * Indicates a significant difference with respect to Gen, genotype, and Age, age (DIV).

the overall contribution of GluN2B subunit-containing NMDARs to the NMDA-induced current would be smaller in L825V/+ neurons compared with +/+ neurons; thus, the degree of ifenprodil inhibition would be lower. However, the difference in the degree of ifenprodil inhibition of NMDAR responses recorded from +/+ and L825V/+ neurons was not significant (ANOVA: $p = 0.07$ for genotype), suggesting similar relative contributions of GluN2A and GluN2B subunits to the whole-cell currents in +/+ and L825V/+ neurons at any given DIV.

Accelerated deactivation of NMDAR-eEPSC in L825V/+ neurons
To investigate the synaptic population of ionotropic glutamate receptors, we used microisland cultures to record NMDAR-mediated or AMPAR-mediated components of eEPSCs,

pharmacologically isolated using NBQX or AP-5, respectively (see Materials and Methods for details). eEPSCs could usually be observed at the earliest at 6 DIV. Peak current densities of NMDAR-eEPSCs recorded from +/+ and L825V/+ neurons increased with DIV with no genotype difference (Fig. 4A; ANOVA: $p < 0.001$ for age, $p = 0.33$ for genotype). Similarly, peak current densities of AMPAR-eEPSCs recorded from +/+ and L825V/+ neurons increased with DIV with no genotype difference (Fig. 4B; ANOVA: $p < 0.001$ for age, $p = 0.78$ for genotype). The analysis of the time course of NMDAR-eEPSCs showed that the kinetics of deactivation accelerated with DIV in neurons of both genotypes (Fig. 4C; ANOVA: $p < 0.001$ for age). Overall these observations are consistent with the expected synaptic developmental changes. Interestingly, in L825V/+ neurons, the NMDAR-eEPSC deactivation kinetics were ~20%

faster compared with +/+ neurons at all DIV (Fig. 4C, ANOVA: $p < 0.001$ for genotype), suggesting a decreased relative contribution of the GluN2B subunit to NMDAR-eEPSCs.

We next used ifenprodil to examine the subunit composition of synaptic NMDARs. In contrast to whole-cell NMDA-induced currents (Fig. 3D) and despite the observed acceleration of NMDAR-eEPSCs with DIV (Fig. 4C), the degree of ifenprodil (3 µM) inhibition of peak NMDAR-eEPSCs did not appreciably change with DIV (Fig. 4D; ANOVA: $p = 0.69$ for age; Gray et al., 2011). Importantly, ifenprodil (3 µM) inhibited peak NMDAR-eEPSCs less in L825V/+ than in +/+ neurons (Fig. 4D; ANOVA: $p = 0.001$ for genotype). Together the results indicate

that in L825V/+ neurons, there is a reduced relative contribution of GluN2B subunit-containing receptors to NMDAR-eEPSCs, but not to NMDA-induced whole-cell currents, suggesting possible differences between the impact of the GluN2B(L825V) variant on the subunit composition of synaptic versus extrasynaptic NMDARs.

Synapse development in +/+ and in L825V/+ neurons
NMDARs play a role in the development and long-term stabilization of synapses and spines (Alvarez et al., 2007), so chronic functional changes in NMDAR signaling due to the presence of the GluN2B(L825V) variant may influence synapse development.
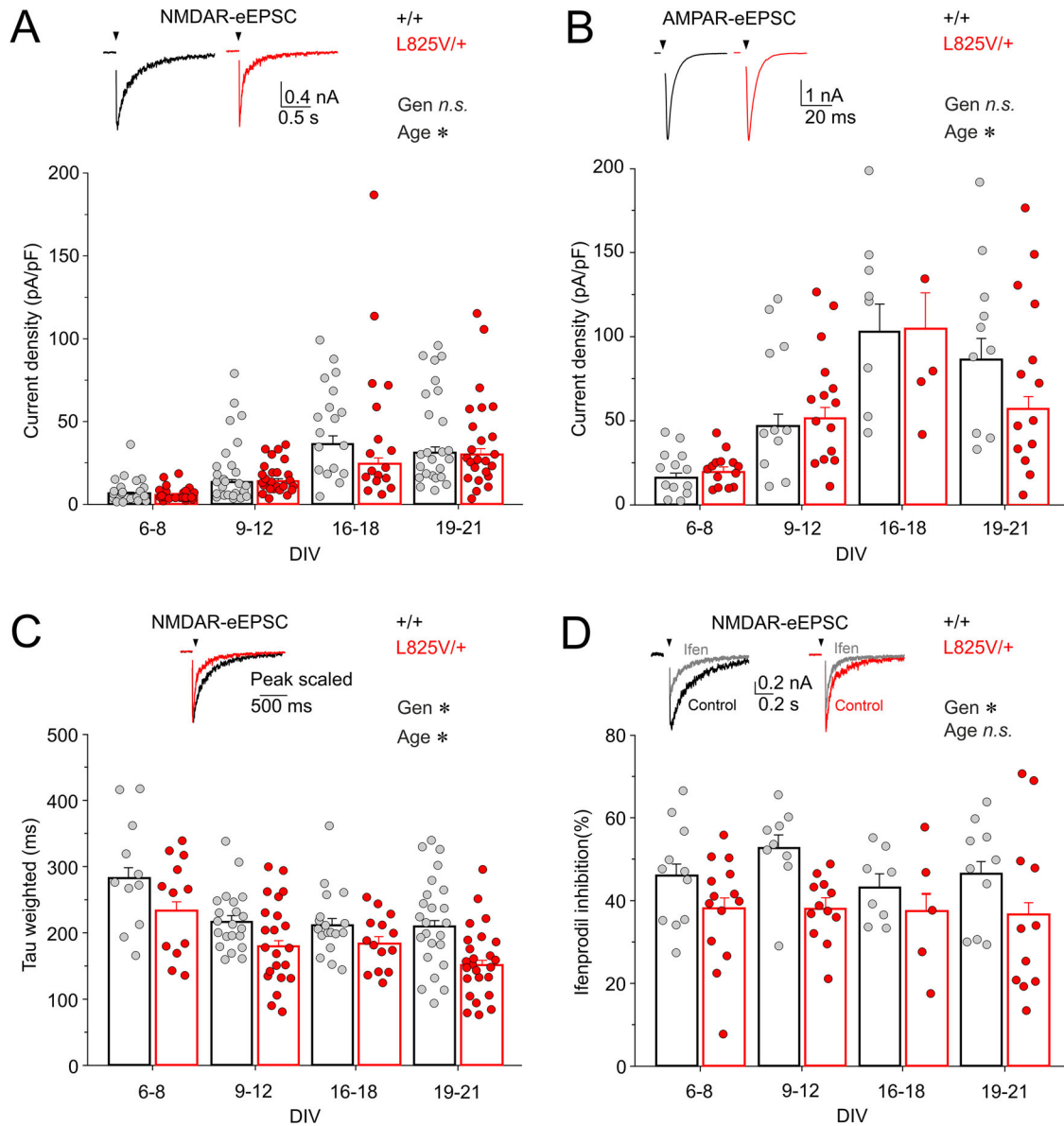

Figure 4. NMDAR-eEPSCs in L825V/+ neurons have faster deactivation and lower sensitivity to ifenprodil inhibition. Scatter plots show the distribution of peak current density of NMDAR-eEPSCs (*A*) and AMPAR-eEPSCs (*B*) recorded from individual +/+ (gray symbols) or L825V/+ (red symbols) neurons by age in vitro; bar graphs show mean ± SEM for each genotype and age group. Insets show representative eEPSCs recorded from +/+ (black) and L825V/+ (red) neurons at 7 and 8 DIV, respectively, for NMDAR-eEPSCs, and at 7 and 11 DIV, respectively, for AMPAR-eEPSCs. *C*, The scatter plot shows the distribution of weighted deactivation time constants (tau weighted) of NMDAR-eEPSCs recorded from individual +/+ or L825V/+ neurons by age in vitro; the bar graph shows mean ± SEM for each genotype and age group. Inset shows scaled NMDAR-eEPSCs from a +/+ (black, 7 DIV) and a L825V/+ neuron (red, 8 DIV). *D*, The scatter plot shows the distribution of ifenprodil (3 µM) inhibition of peak NMDAR-eEPSCs recorded in individual neurons by age in vitro; the bar graph shows mean ± SEM for each genotype and age group. Inset shows control NMDAR-eEPSCs and the effect of 3 µM ifenprodil (shown in gray) recorded from a +/+ (black) and L825V/+ (red) neuron cultured for 7 and 8 DIV, respectively. Data (obtained from $n = 5$–26 neurons from 3 to 13 animals per group) were power transformed and tested using ANOVA. * Indicates a significant difference with respect to Gen, genotype, and Age, age (DIV).

The amplitude of the AMPAR-eEPSC is a function of the number of stimulated synapses, the probability of glutamate release, and the average AMPAR density at individual synapses. To examine potential genotype-related changes in these parameters over the course of development, we recorded mEPSCs from +/+ and L825V/+ neurons at different DIV. Spontaneous EPSCs recorded in single-neuron microisland cultures correspond to mEPSCs because action potential-dependent transmitter release is prevented by clamping the autaptic neuron at −70 mV (Mennerick and Zorumski, 1995). An AMPAR-mEPSC represents the response to a spontaneously released vesicle detected by postsynaptic receptors at a single synapse. AMPAR-mEPSC amplitude provides information about postsynaptic AMPAR density/function, and AMPAR-mEPSC frequency depends on the number of synapses present and their presynaptic release properties. The amplitude of AMPAR-mEPSCs recorded from +/+ and L825V/+ neurons increased with DIV with no genotype difference (Fig. 5A,B; ANOVA: $p < 0.001$ for age, $p = 0.84$ for genotype). The frequency of AMPAR-mEPSCs also increased with DIV and was slightly higher in L825V/+ compared with +/+ neurons (Fig. 5C;

ANOVA: $p < 0.001$ for age, $p = 0.03$ for genotype), suggesting that the number of synapses and/or the probability of glutamate release is higher in the presence of the L825V variant. The ratio of the current amplitudes of AMPAR-eEPSCs and AMPAR-mEPSCs from an individual neuron can provide information about the number of synapses releasing glutamate in this neuron following a stimulus. The estimated number of synapses releasing glutamate following a stimulus increased with DIV similarly for both genotypes (Fig. 5D; ANOVA: $p < 0.001$ for age, $p = 0.48$ for genotype). The mEPSC data suggest that, over the course of early development, functional changes in NMDAR signaling due to the presence of a single allele of the GluN2B(L825V) variant may have secondary effects on synapse development.

GluN2B(L825V) subunit has unchanged surface expression and synaptic localization

Within the assembled receptor, GluN2 subunits are necessary for glutamate-dependent activation, but they are also crucial for subcellular trafficking (Horak et al., 2014; Vieira et al., 2020). Given our observation that whole-cell and synaptic
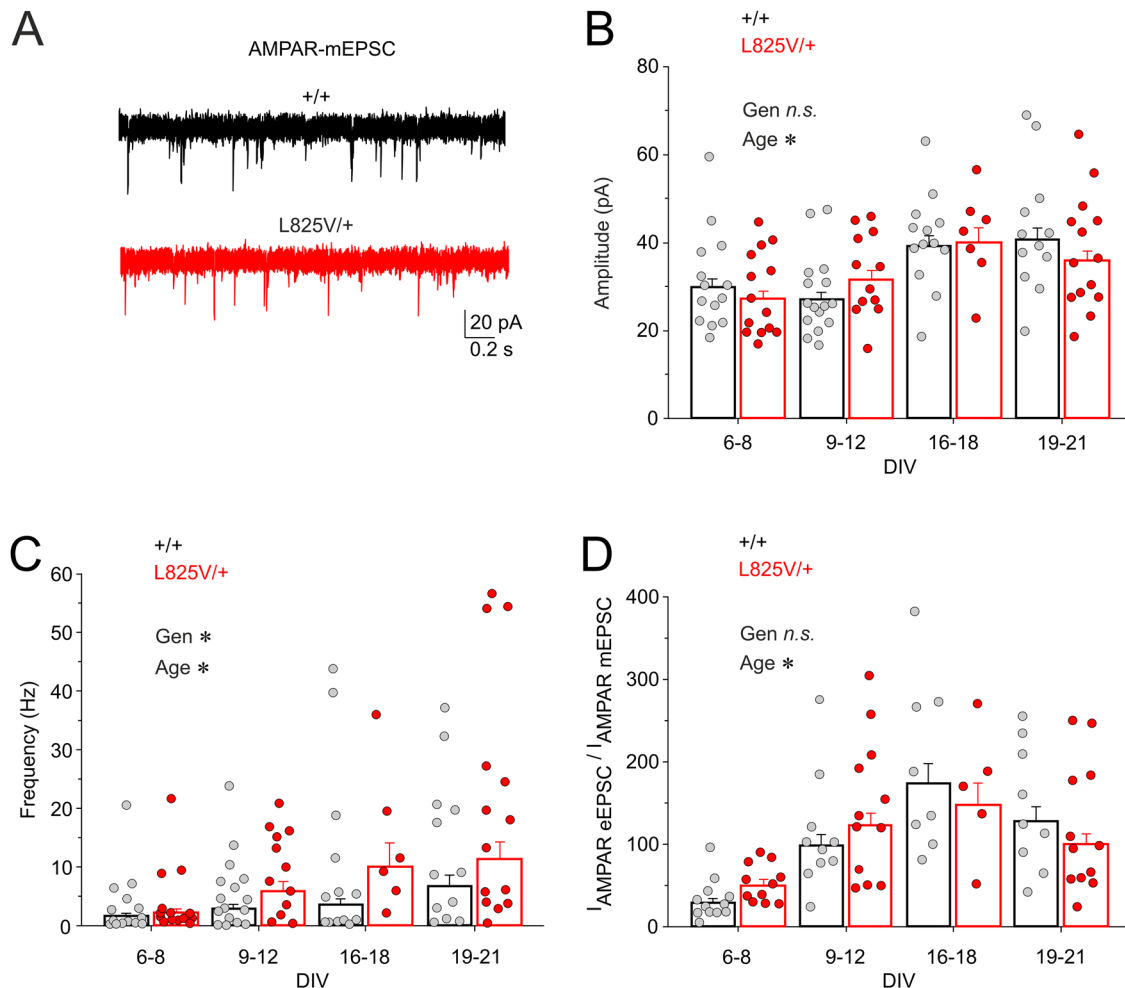

Figure 5. Properties of AMPAR-mEPSCs in +/+ and L825V/+ neurons. **A,** Representative recording of AMPAR-mEPSCs from single-neuron microisland cultures prepared from +/+ or L825V/+ animals and maintained for 21 DIV. **B,** The scatter plot shows the distribution of mean AMPAR-mEPSC current amplitudes recorded from individual +/+ and L825V/+ autaptic neurons (each point represents mean AMPAR-mEPSC amplitude from a 2 min recording period) by age in vitro; the bar graph shows mean ± SEM for each genotype and age group. **C,** The scatter plot shows the distribution of AMPA-mEPSC frequency recorded from individual +/+ and L825V/+ autaptic neurons by age in vitro; the bar graph shows mean ± SEM for each genotype and age group. **D,** The scatter plot shows the distribution of the ratio of peak AMPAR-eEPSC current amplitude and mean AMPAR-mEPSC current amplitudes recorded from individual +/+ and L825V/+ neurons by age in vitro; the bar graph shows mean ± SEM for each genotype and age group. Data (obtained from $n = 5$–16 neurons from 3 to 7 animals per group) were power transformed and tested using ANOVA. * indicates a significant difference with respect to Gen, genotype, and Age, age (DIV).

NMDAR-mediated currents are differently affected by the GluN2B(L825V) variant (Figs. 3, 4), we next asked whether NMDARs containing the GluN2B(L825V) subunit have altered trafficking or subcellular localization. We infected cultured mouse hippocampal neurons with a lentivirus containing hGluN2B WT or hGluN2B(L825V) subunit tagged with eGFP. Ten days following the infection, we used immunocytochemistry followed by fluorescence microscopy to detect the cell surface and intracellular protein levels of eGFP-tagged GluN2B (Fig. 6A). Consistent with our previous results on NMDARs expressed in HEK293T cells (Vyklicky et al., 2018), the quantitative analysis of images of cultured hippocampal neurons indicated no difference in the delivery of receptors containing the eGFP-hGluN2B WT or eGFP-hGluN2B(L825V) subunit to the cell surface at the soma [Fig. 6B; the ratio of soma surface/intracellular fluorescence intensity of eGFP-hGluN2B(L825V) normalized to WT was 1.05 ± 0.08, $p = 0.65$, LSD method]. Similarly, no difference was found between the relative cell surface expression of eGFP-hGluN2B WT and eGFP-hGluN2B(L825V) in dendritic spines, identified based on the staining for a synaptic marker PSD-95 [Fig. 6C; data averaged from five spines per neuron, located on five separate dendritic segments; the ratio of spine surface/intracellular fluorescence intensity of GFP-hGluN2B(L825V) normalized to WT was 1.08 ± 0.03, $p = 0.1$, LSD method].

To further characterize the synaptic localization of receptors containing the hGluN2B(L825V) subunit, we selected one 20 µm segment of dendrite (secondary or above) per neuron and calculated Mander's overlap coefficient between the surface eGFP-hGluN2B and PSD-95 labeling and the percentage of surface eGFP-hGluN2B pixels overlapping with PSD-95 (see Materials and Methods). Both Mander's overlap coefficient [Fig. 6D; eGFP-hGluN2B WT: 0.93 ± 0.02, eGFP-hGluN2B(L825V): 0.95 ± 0.02, $p = 0.86$, LSD method] and the percentage of overlapping pixels [Fig. 6E; eGFP-hGluN2B WT: $58.8 \pm 1.6\%$, eGFP-hGluN2B(L825V): $63.9 \pm 2.0\%$, $p = 0.05$, LSD method] assessed from dendritic staining were comparable between neurons transfected with eGFP-hGluN2B WT or eGFP-hGluN2B(L825V) subunits.

Next we used super-resolution STED microscopy to quantify Mander's overlap coefficient and the percentage of overlapping pixels between the surface eGFP-hGluN2B and PSD-95 labeling (see Materials and Methods) assessed from ROIs of dendritic spines (one per neuron). Again, both measures were comparable between neurons transfected with eGFP-hGluN2B WT or eGFP-hGluN2B(L825V) subunits [Fig. 6F–H; Mander's overlap coefficient: eGFP-hGluN2B WT: 0.88 ± 0.02, eGFP-hGluN2B(L825V): 0.91 ± 0.02, $p = 0.41$, LSD method; percentage of overlapping pixels: eGFP-hGluN2B WT: $74.96 \pm 3\%$, eGFP-hGluN2B(L825V): $81.32 \pm 3\%$, $p = 0.1$, LSD method]. These results indicate that the L825V variant in the GluN2B subunit does not impact the synaptic localization of NMDARs containing this subunit.

Protein expression in the hippocampus of L825V/+ mice

To further investigate possible effects of the GluN2B(L825V) variant on other components of glutamatergic signaling, we performed mass spectrometry proteomic analysis of whole hippocampus samples from adult male +/+ and L825V/+ mice. After filtering raw data using the criteria described in the Materials and Methods, we obtained 5,454 proteins for further analysis. We found that the presence of one Grin2b^{L825V} allele in L825V/+ mice has a minimal effect on the expression levels of >5,000 detected proteins compared with +/+ mice (Fig. 7). We detected and analyzed the expression of GluN1, GluN2A, and GluN2B subunits of NMDARs and also GluA1-3 subunits of AMPARs and GluK2 subunit of kainate receptors. All glutamate receptor subunits examined were without an expression shift, so the functional effects we observed are unlikely to originate from possible global compensatory changes in the expression of different glutamate receptor subunits. From the differentially expressed proteins, several collagens (CO1A1, CO6A1, CO1A2) were upregulated in the variant strain showing about a twofold increase in the level of expression. CO1A1 is present in all cell compartments and in the extracellular matrix and could play a role in neural growth. Overall, based on our mass spectrometry data, the changes observed in L825V/+ mice do not seem to be associated with global changes in protein expression. Any changes in protein expression or distribution potentially associated with the presence of the GluN2B(L825V) variant may be more localized and specific.

Behavioral assessment of L825V/+ mice

To model the effects of the human ID-/ASD-associated de novo variant GluN2B(L825V) at the system level, we explored how the presence of a single Grin2b^{L825V} allele affects mouse behavior. Homozygous Grin2b$^{L825V/L825V}$ mice showed perinatal or early postnatal death, similar to mice with homozygous Grin2b deletion (Kutsuwada et al., 1996; Sprengel et al., 1998). In contrast, heterozygous L825V/+ mice were born at the expected Mendelian ratios and showed normal survival. We applied a battery of behavioral tests to male and female +/+ and L825V/+ mice at 9–15 weeks of age, focusing on parameters relevant to the ID/ASD diagnosis of the patient heterozygous for the GRIN2B^{L825V} variant, such as sensory processing, cognition and cognitive flexibility, and anxiety.

Open-field test, providing information on animal activity and anxiety levels in a novel environment, revealed a sex-dependent behavioral phenotype of L825V/+ mice (Fig. 8A,B). L825V/+ males traveled shorter distances than +/+ males (17.3 ± 1.7 m, $n = 11$ vs 22.5 ± 1.6 m, $n = 10$; $p = 0.01$, LSD method) with a lower average speed, spent less time in the anxiogenic center of the maze (62.4 ± 10 s, $n = 11$ vs 99.63 ± 11 s, $n = 10$; $p = 0.047$, LSD method), and visited the center less frequently than +/+ males (34.2 ± 4, $n = 11$ vs 46.7 ± 4, $n = 10$; $p = 0.02$, LSD method). In contrast, L825V/+ females and +/+ females had similar activity and zone exploration parameters (distance traveled: 24.6 ± 1 m, $n = 11$ vs 23.3 ± 2 m, $n = 12$; $p = 0.6$, LSD method; center permanence: 77.7 ± 10 s, $n = 11$; 87 ± 10 s, $n = 12$; $p = 0.43$, LSD method; center entries: 42.9 ± 4, $n = 11$; 44.2 ± 4, $n = 12$; $p = 0.75$, LSD method). Further, we tested animals' sensorimotor gating as measured by the PPI of the startle reflex. The PPI test showed that in L825V/+ mice, the startle response decrease at the lower prepulse intensities was attenuated compared with +/+ mice; however, the differences reached statistical significance only in males (Fig. 8C; effect of genotype on PPI in males: $p < 0.001$, ANOVA; in females: $p = 0.10$, ANOVA). These results indicate a sex-dependent impairment of sensorimotor gating in L825V/+ mice, preferentially affecting males. We also tested simple associative learning using cued and contextual fear conditioning. In both conditioning paradigms, freezing time was independent of genotype (Fig. 8D; males: $p = 0.065$, ANOVA; females: $p = 0.852$, ANOVA). Throughout the testing period, when +/+ and L825V/+ littermates were kept together in home cages, we frequently observed male aggression, typically initiated by L825V/+ mice.
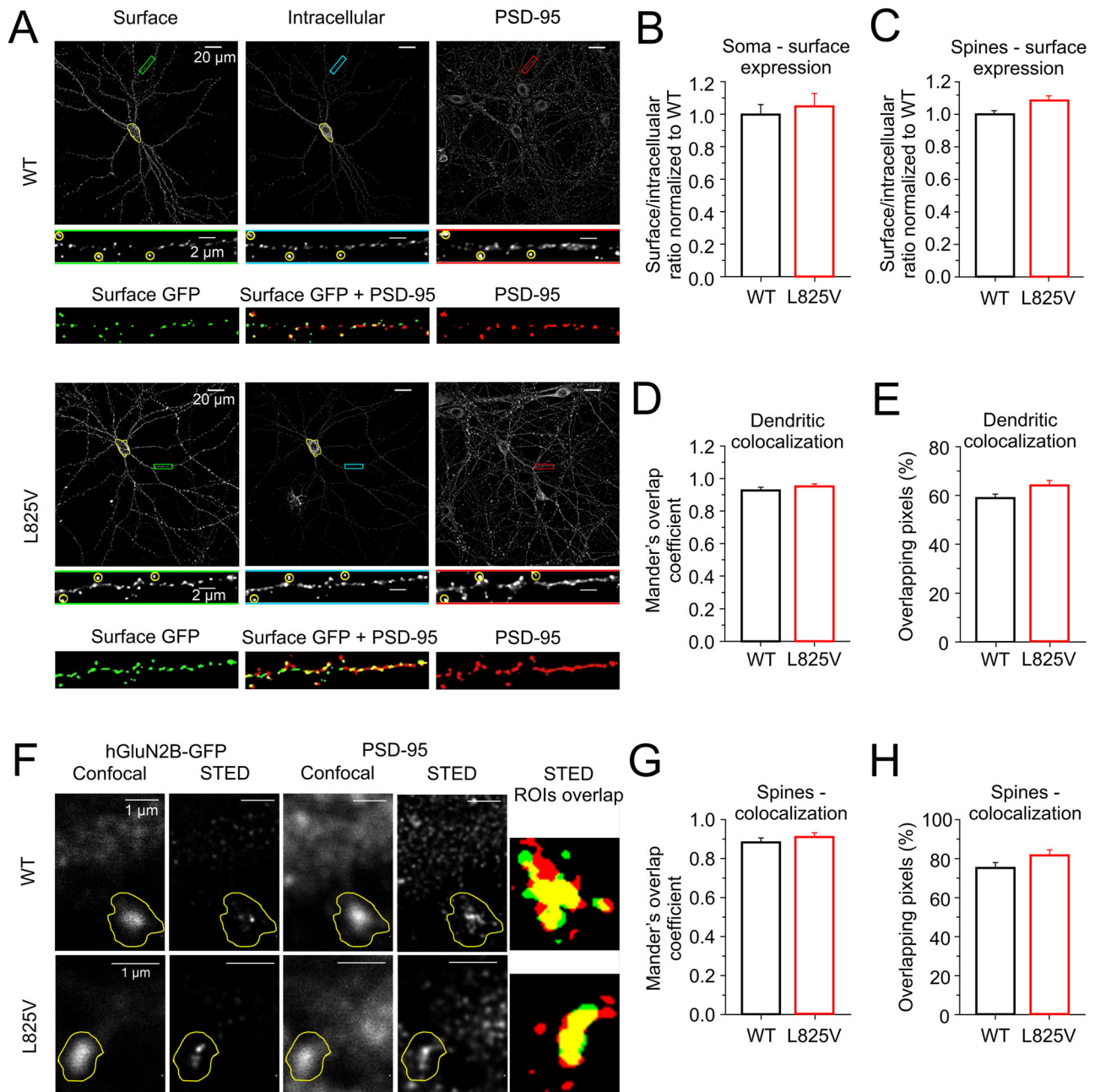
Figure 6. Cell surface expression and synaptic localization of NMDARs containing the eGFP-hGluN2B WT or eGFP-hGluN2B(L825V) subunit. ***A***, Representative images (maximum intensity projection) of mouse hippocampal neurons (14 DIV) showing surface and intracellular immunostaining for WT or L825V eGFP-hGluN2B subunits and total immunostaining for PSD-95. The area highlighted in yellow indicates the soma of the neuron. Green, blue, and red rectangles indicate secondary dendrites and are also shown below at a higher magnification (highlighted areas show examples of dendritic spines used for analysis). The bottom row shows thresholded surface receptors (green) and PSD-95 (red) with their composite image used to calculate the overlap of surface receptors with PSD-95. ***B, C***, Summary of the relative cell surface expression of NMDARs containing WT or L825V eGFP-hGluN2B measured at the soma (***B***) and in dendritic spines (***C***), both expressed as the ratio of surface/intracellular fluorescence intensity normalized to WT. ***D, E***, Summary of the colocalization analysis of dendritic surface WT or L825V eGFP-hGluN2B with PSD-95 assessed by Mander's overlap coefficient (***D***) and by the percentage of overlapping pixels (***E***). ***F***, Representative images of dendritic spines showing immunostaining for WT or L825V eGFP-hGluN2B and for PSD-95 by confocal and super-resolution STED microscopy. The areas marked in yellow indicate ROIs used in the colocalization analysis. Color images on the right show the overlap of STED deconvolved ROIs after Huang segmentation between eGFP-hGluN2B (green) and PSD-95 (red) labeling. ***G***, Summary of the colocalization analysis of WT or L825V eGFP-hGluN2B with PSD-95 assessed by Mander's overlap coefficient. ***H***, Summary of the colocalization analysis determined as the percentage of pixels of surface WT or L825V eGFP-hGluN2B labeling overlapping with PSD-95. The summary data are presented as the mean ± SEM; for ***B–E***, $n = 22–40$ neurons from 4 to 10 cultures; for ***G, H***, $n = 15–17$ neurons from two cultures. No significant differences were found between WT and L825V eGFP-hGluN2B data shown in ***B–E*** and ***G*** and ***H***.

Next, we tested animals' cognitive performance using IntelliCages, a system that provides an approach to testing group-housed animals without human impact. The IntelliCages have door-guarded entries to drinking water reservoirs, and the drinking responses of individual animals are tracked via subcutaneous radio-frequency transponders. Testing proceeded in phases as described in the Materials and Methods. In the initial free adaptation phase, the novelty response measured by the
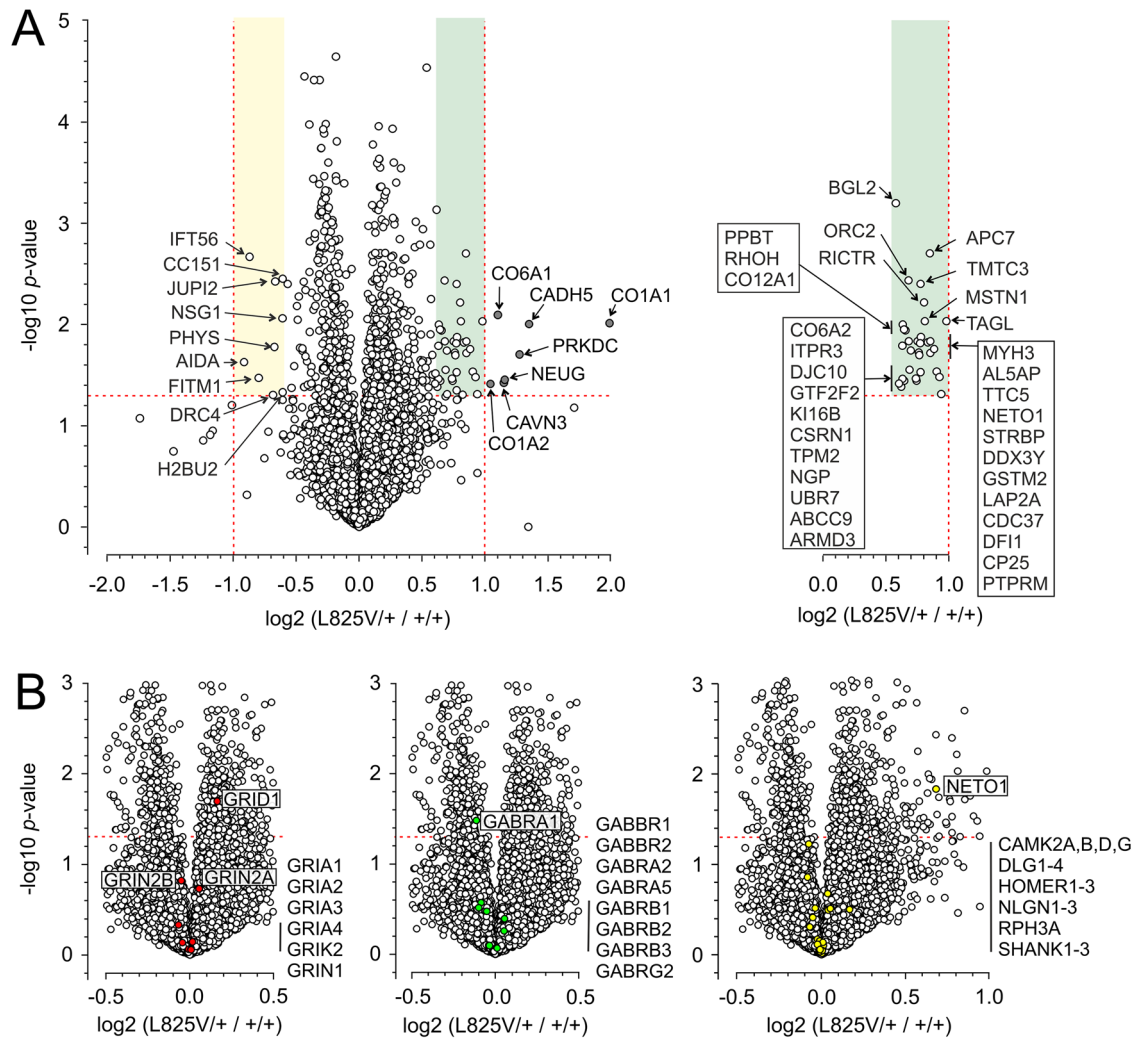
Figure 7. Analysis of protein levels in +/+ and L825V/+ mouse hippocampus. ***A***, The volcano plot showing proteomics data. The abscissa displays negative (downregulated) and positive (upregulated) fold changes in the ratio of the protein levels found in the hippocampi of L825V/+ relative to +/+ mice. The statistical significance (-log of p-values) is indicated on the ordinate. The dashed horizontal line shows the p-value of 0.05 cutoff, and the two vertical dashed lines indicate twofold down-/upregulation of the protein level. The gray symbols show proteins expressed significantly ($p < 0.05$) more (greater than twofold) in the hippocampi of L825V/+ compared with +/+ mice. The area highlighted in green in ***A*** is also shown on the right with individual detected proteins labeled. ***B***, The same data as in ***A***; highlighted in red are the AMPAR, kainate receptor, and NMDAR subunits; highlighted in green are the GABA$_A$R subunits; highlighted in yellow are the selected synaptic proteins.

latency of the first visit to a drinking corner, the latency of the first nosepoke, and the latency of the first lick attempt was significantly prolonged in L825V/+ animals compared with +/+ animals (Fig. 9A), to different extents in males and females. In the free adaptation phase, L825V/+ mice of both sexes made fewer drinking corner visits throughout the circadian cycle, confirming the hypoactivity of L825V/+ animals (Fig. 9B; effect of genotype in males: $p < 0.03$, ANOVA; in females: $p < 0.001$, ANOVA).

In experiments involving the drinking session, when access to water was limited to two 2 h sessions every day, it was apparent that L825V/+ males became aggressive, and the testing of males in the IntelliCages had to be terminated with regard to animal welfare. In subsequent sessions, only females were tested (Fig. 9C). There was no difference between females of different genotypes in place preference learning ($p = 0.18$, ANOVA). However, in place preference reversal learning, a task demanding cognitive flexibility, L825V/+ females performed significantly more poorly than +/+ females ($p < 0.001$, ANOVA). L825V/+ females also showed a significant working memory impairment

in the patrolling task (Fig. 9C; $p < 0.001$, ANOVA). Together, the IntelliCage experiments highlighted the issue of L825V/+ male anxiety/aggression, and the results demonstrated a behavioral phenotype of L825V/+ females characterized by overall hypoactivity and specific cognitive deficits.

Discussion

We have used a multidisciplinary approach to characterize the pathogenicity of the de novo variant *GRIN2B*^{L825V} found in a patient with ID/ASD (Awadalla et al., 2010; Tarabeux et al., 2011). Using a heterologous expression system and a knock-in mouse line carrying this variant in the *Grin2b* gene, we characterized the effects of the GluN2B(L825V) subunit at the molecular, cellular, synaptic, and behavioral levels. Our functional study demonstrates a reduced P_o of di- and triheteromeric receptors containing the GluN2B(L825V) subunit. In primary hippocampal neurons prepared from L825V/+ mice, NMDA-induced whole-cell currents were smaller than in +/+ neurons, and NMDAR-eEPSCs had faster deactivation and were less sensitive
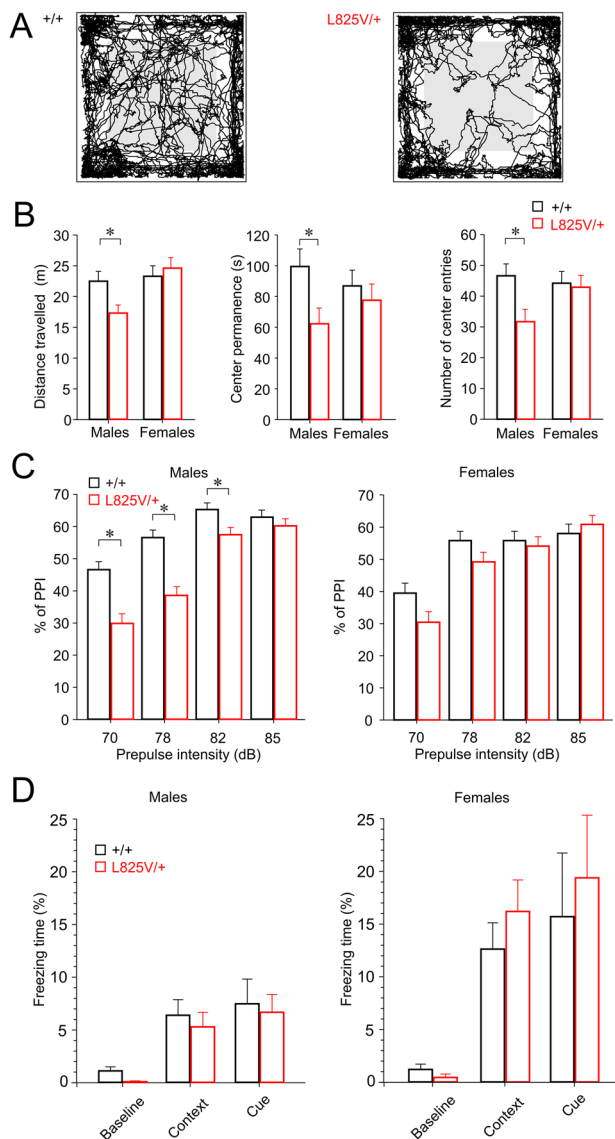
Figure 8. Adult L825V/+ mice display sex-dependent hypoactivity, anxiety, and impaired sensorimotor gating, preferentially affecting males. **A**, Representative locomotion track traces of +/+ and L825V/+ mice in the open-field test. **B**, Quantification of the total distance traveled, center permanence, and the number of center entries. **C**, Quantification of the % inhibition of the startle response as a function of prepulse intensity. **D**, Freezing time (%) in response to context or cue (contextual or cued fear conditioning test). Data [obtained from $n = 10$–12 animals (from 5 to 7 litters) per group] are presented as mean ± SEM and were analyzed by ANOVA followed by post hoc tests using the LSD method. * Indicates a significant genotype difference.

to the GluN2B subunit-selective inhibitor ifenprodil. Behavioral tests performed on adult L825V/+ mice showed sex-dependent changes preferentially affecting males, including hypoactivity, anxiety, and impaired sensorimotor gating; propensity for aggression precluded full examination of cognitive function in males. Female L825V/+ mice showed cognitive deficits, particularly in tasks that were more demanding or required cognitive flexibility.

Previous electrophysiological examination has shown that the EC_{50} for glutamate and glycine, desensitization, the IC_{50} for Mg^{2+}, proton inhibition, deactivation after brief glutamate application, and surface expression are not changed for recombinant diheteromeric GluN1/GluN2B(L825V) compared with GluN1/GluN2B

receptors (Platzer et al., 2017; Amin et al., 2018; Vyklicky et al., 2018). We have shown that diheteromeric GluN1/GluN2B(L825V) receptors have a loss-of-function phenotype due to a strongly reduced P_o, and they possess a remarkably high sensitivity to potentiating steroids (Vyklicky et al., 2018; Kysilov et al., 2022). Here we have characterized the P_o of triheteromeric receptors. We show that the presence of a single GluN2B(L825V) subunit in GluN1/GluN2B/GluN2B(L825V) receptors results in P_o values intermediate between diheteromeric WT GluN1/GluN2B and diheteromeric variant GluN1/GluN2B(L825V) receptors. The reduction of P_o was also observed for triheteromeric GluN1/GluN2A/GluN2B(L825V) receptors (Fig. 1). MD simulations suggest greater mobility of the TMD helices in the diheteromeric GluN1/GluN2B(L825V) closed receptor, suggesting a partial loss of fidelity in the inter-residue interaction network in the TMD compared with the WT GluN1/GluN2B receptor. This may lead to a less efficient response to the rotation and pulling induced by the agonist-bound extracellular domains during the opening transition.

The current density induced by NMDA application in hippocampal L825V/+ neurons is ∼60% of that found in +/+ neurons (Fig. 3C). This result may be solely due to the reduced P_o of di- and triheteromeric receptors containing the GluN2B(L825V) subunit. However, we have also considered the possibility that the diminished whole-cell NMDAR current density may be partly due to the reduced delivery of GluN2B(L825V) or other NMDAR subunits to the cell surface. Previous studies have shown that decreased surface protein levels play an important role in the functional effects of some disease-associated missense NMDAR variants (Serraz et al., 2016; Swanger et al., 2016; Liu et al., 2017; W. Chen et al., 2017; Vyklicky et al., 2018; Sceniak et al., 2019; Kysilov et al., 2022). Our results, however, provide no evidence to support the idea that decreased cell surface GluN2B protein levels contribute to the reduced NMDAR current density in L825V/+ neurons. First, we found no difference in the degree of ifenprodil inhibition of whole-cell NMDAR currents in L825V/+ versus +/+ neurons (Fig. 3D). This suggests that there may actually be an opposite effect, an overexpression of di- or triheteromeric NMDARs containing the GluN2B subunit to compensate for the presumed diminished current due to the reduced P_o of receptors containing the GluN2B(L825V) subunit. Further, quantitative immunofluorescence analysis of the GFP-tagged hGluN2B or hGluN2B(L825V) subunit overexpressed in cultured hippocampal neurons showed no effect of the variant on the subunit cell surface expression (Fig. 6B). Finally, we detected no global difference in the expression level of the GluN2B subunit in the hippocampal tissue of L825V/+ and +/+ mice (Fig. 7B). Similarly, we found no changes in the expression of other NMDAR subunits, including the principal subunit GluN1.

In contrast to whole-cell NMDA-induced currents, NMDAR-eEPSCs in L825V/+ neurons were significantly less sensitive to ifenprodil inhibition than NMDAR-eEPSCs in +/+ neurons. The presence of the L825V variant caused no change in peak NMDAR-eEPSC, but significantly accelerated eEPSC deactivation (Fig. 4). Together, these findings are consistent with a reduced relative GluN2B subunit contribution to synaptic currents, possibly simply due to the reduced P_o of NMDARs containing the GluN2B(L825V) subunit. Indeed, based on the fluorescence microscopy results, the hGluN2B(L825V) subunit is delivered to synapses as efficiently as the WT hGluN2B. Our observations are in line with recent studies of synaptic effects of different GluN2 subunit variants introduced to neurons in
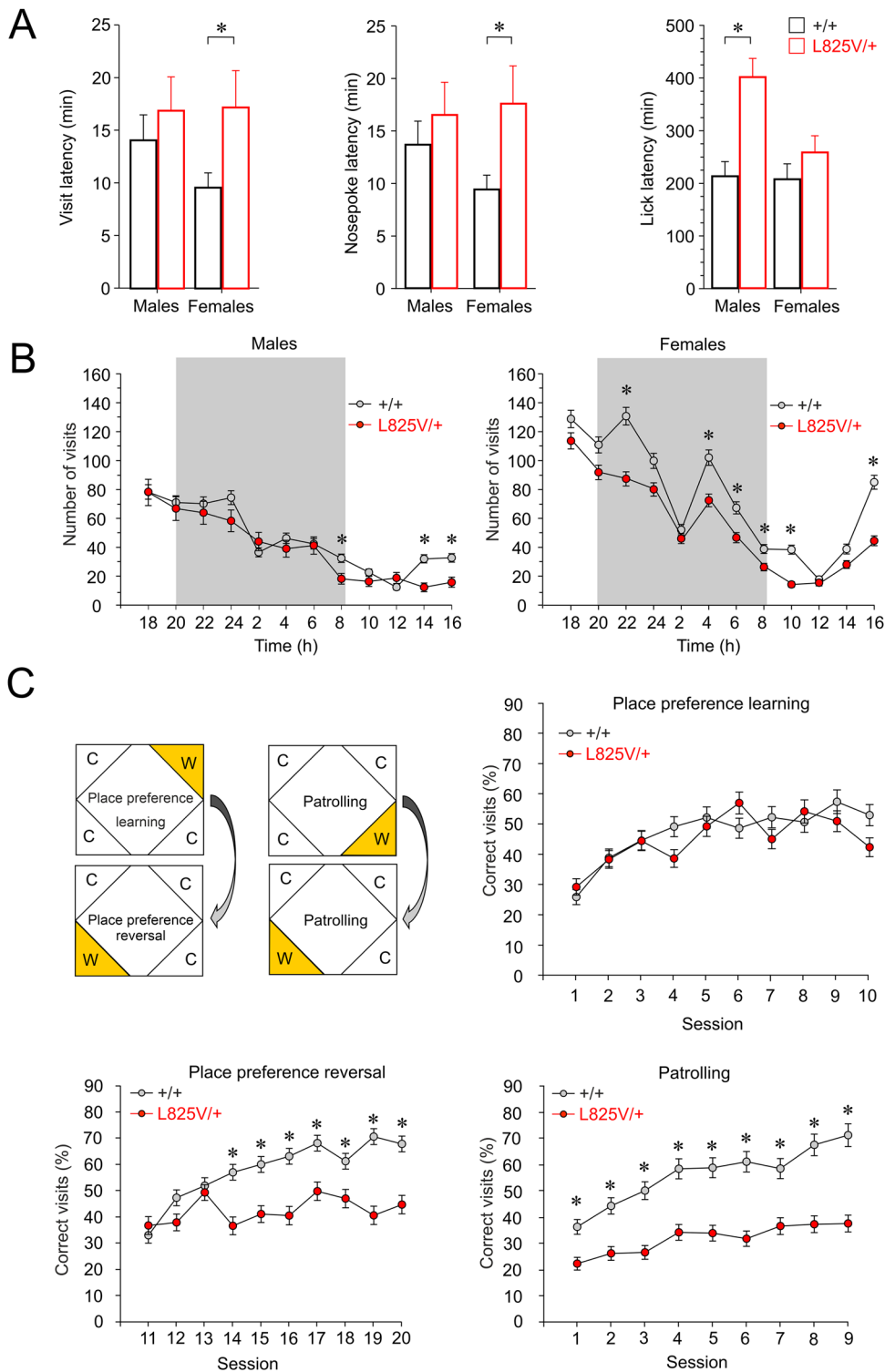
Figure 9. Behavioral phenotyping of L825V/+ mice in the IntelliCage system. **A**, First visit, nosepoke, and lick attempt latency at the corner chambers after introducing animals to the IntelliCage. **B**, The number of visits during the initial free adaptation phase lasting 4 consecutive days (all corners had doors open and mice had free access to water). **C**, Trial design for the different behavioral tasks: *C*, unconditionally closed; *W*, water available at the designated corner during the drinking sessions (21:00–23:00 and 3:00–5:00). Graphs show learning performance in the place preference, place preference reversal, and patrolling tests. Each plot represents the session score based on the proportions of visits to the correct corner (in %). Data [obtained from $n = 9–10$ animals (from 4 to 7 litters) per group] are presented as mean ± SEM and were analyzed by ANOVA followed by post hoc tests using the LSD method. * Indicates a significant genotype difference.

organotypic cultures (Elmasri et al., 2022a,b). Specifically, GluN2B subunit variants were consistently associated with accelerated eEPSC deactivation, presumably reflecting greater relative contribution of diheteromeric GluN1/GluN2A and triheteromeric GluN1/GluN2A/GluN2B receptors to synaptic transmission in the presence of disease-associated GluN2B subunit

variants (Elmasri et al., 2022b). Given that the time course of the NMDAR-eEPSC, and the associated Ca^{2+} influx, is an important determinant of circuit function, this synaptic phenotype may underlie the neurodevelopmental pathology associated with the GluN2B(L825V) variant at the circuit and system level.

Adult mice heterozygous for the ID/ASD-associated *Grin2b*^*L825V*^ variant exhibit sex-specific hypoactivity and increased anxiety in the open-field test and impaired sensorimotor gating; these traits are observed more prominently in males. The observed aggressive behavior of L825V/+ male mice precluded their detailed cognitive assessment in the IntelliCage system, but IntelliCage data from L825V/+ females demonstrate hypoactivity, reduced cognitive flexibility, and impaired working memory compared with +/+ females. This behavioral phenotype is in line with the most prominent diagnosis of ID/ASD associated with *GRIN2B* variants (Awadalla et al., 2010; Tarabeux et al., 2011; Platzer et al., 2017).

To our knowledge, only one other mouse model of *GRIN2B*-related neurodevelopmental disorder has been generated and described to date, a transgenic mouse line heterozygous for *Grin2b*^*C456Y*^, corresponding to a de novo variant identified in a male patient with ID/ASD (Shin et al., 2020). Previous assessment of this ABD variant in recombinant diheteromeric GluN1/GluN2B(C456Y) receptors revealed a loss-of-function phenotype at the receptor level primarily due to reduced receptor surface expression (Swanger et al., 2016). NMDAR-eEPSCs in neurons from *Grin2b*^*C456Y/+*^ mice had reduced peak amplitudes as well as faster deactivation kinetics and were less sensitive to ifenprodil inhibition. *Grin2b*^*C456Y/+*^ mice also had reduced levels of GluN2B protein in the hippocampus (Shin et al., 2020). Behaviorally, *Grin2b*^*C456Y/+*^ mice showed hypoactivity and reduced anxiety, but normal cognition and social behavior (Shin et al., 2020). Comparison with our results suggests that different receptor-level functional changes may lead to slightly different synaptic-, cellular-, and system-level outcomes, underscoring the importance of animal models for evaluating the impact of different *GRIN* gene variants.

Other genetic or pharmacological mouse models of ASD (including *Cacna1c*, *Tsc1*, *Cntnap2*, or *Shank3* transgenic mice, or mice exposed to prenatal zinc deficiency) show behaviors characterized by cognitive deficits, anxiety, and male aggression, among other traits [for review, see Bey and Jiang (2014) and Sauer et al., (2022)], similar to the behavioral profile of our mouse model of *Grin2b* variant-related ASD. The observed behavioral changes in L825V/+ mice are also consistent with the behavioral manifestation of ASD in humans (Hu et al., 2016). Significant early cognitive impairment and hypoactivity were found in children diagnosed with ASD (Mayes et al., 2023). There is a high prevalence of challenging behaviors, including aggression, in children diagnosed with ASD, and anxiety is also a common concern (White et al., 2009; Hattier et al., 2011).

It is challenging to find a clear link between genetic alterations and behavioral impairments. We present evidence that the ID-/ASD-associated variant *GRIN2B*^*L825V*^ causes a loss of function of NMDARs due to their low P_o. Neurons prepared from L825V/+ mice exhibit smaller whole-cell NMDAR currents and NMDAR-eEPSCs with faster deactivation compared with +/+ mice. L825V/+ mice are characterized by several behavioral impairments, most notably limited cognitive flexibility. Further studies will be required to better understand the link between molecular and cellular consequences of *GRIN* gene variants and their clinical implications. Mice carrying the *Grin2b*^*L825V*^ variant may contribute to this effort and serve as a model for the development of potential clinical interventions.

References

Akashi K, Kakizaki T, Kamiya H, Fukaya M, Yamasaki M, Abe M, Natsume R, Watanabe M, Sakimura K (2009) NMDA receptor GluN2B (GluR epsilon 2/NR2B) subunit is crucial for channel function, postsynaptic macromolecular organization, and actin cytoskeleton at hippocampal CA3 synapses. J Neurosci 29:10869–10882.

Al-Hallaq RA, Conrads TP, Veenstra TD, Wenthold RJ (2007) NMDA di-heteromeric receptor populations and associated proteins in rat hippocampus. J Neurosci 27:8334–8343.

Alvarez VA, Ridenour DA, Sabatini BL (2007) Distinct structural and ionotropic roles of NMDA receptors in controlling spine and synapse stability. J Neurosci 27:7365–7376.

Amin JB, Leng X, Gochman A, Zhou HX, Wollmuth LP (2018) A conserved glycine harboring disease-associated mutations permits NMDA receptor slow deactivation and high Ca(2+) permeability. Nat Commun 9:3748.

Amin JB, Moody GR, Wollmuth LP (2021) From bedside-to-bench: what disease-associated variants are teaching us about the NMDA receptor. J Physiol 599:397–416.

Awadalla P, et al. (2010) Direct measure of the de novo mutation rate in autism and schizophrenia cohorts. Am J Hum Genet 87:316–324.

Ayabe S, Nakashima K, Yoshiki A (2019) Off- and on-target effects of genome editing in mouse embryos. J Reprod Develop 65:1–5.

Bar-Shira O, Maor R, Chechik G (2015) Gene expression switching of receptor subunits in human brain development. PLoS Comput Biol 11:e1004559.

Barria A, Malinow R (2005) NMDA receptor subunit composition controls synaptic plasticity by regulating binding to CaMKII. Neuron 48:289–301.

Benke TA, Park K, Krey I, Camp CR, Song R, Ramsey AJ, Yuan H, Traynelis SF, Lemke J (2021) Clinical and therapeutic significance of genetic variation in the GRIN gene family encoding NMDARs. Neuropharmacology 199:108805.

Benner S, Endo T, Endo N, Kakeyama M, Tohyama C (2014) Early deprivation induces competitive subordinance in C57BL/6 male mice. Physiol Behav 137:42–52.

Bey AL, Jiang YH (2014) Overview of mouse models of autism spectrum disorders. Curr Protoc Pharmacol 66:5.66.1–5.66.26.

Brooks BR, et al. (2009) CHARMM: the biomolecular simulation program. J Comput Chem 30:1545–1614.

Cais O, Sedlacek M, Horak M, Dittert I, Vyklicky L Jr (2008) Temperature dependence of NR1/NR2B NMDA receptor channels. Neuroscience 151:428–438.

Cerny J, Bozikova P, Balik A, Marques SM, Vyklicky L (2019) NMDA receptor opening and closing-transitions of a molecular machine revealed by molecular dynamics. Biomolecules 9:546.

Chen W, et al. (2017) GRIN1 mutation associated with intellectual disability alters NMDA receptor trafficking and function. J Hum Genet 62:589–597.

Chen N, Luo T, Raymond LA (1999) Subtype-dependence of NMDA receptor channel open probability. J Neurosci 19:6844–6854.

Doerr S, Harvey MJ, Noe F, De Fabritiis G (2016) HTMD: high-throughput molecular dynamics for molecular discovery. J Chem Theory Comput 12:1845–1852.

Dupuis JP, et al. (2014) Surface dynamics of GluN2B-NMDA receptors controls plasticity of maturing glutamate synapses. EMBO J 33:842–861.

Elmasri M, Hunter DW, Winchester G, Bates EE, Aziz W, Van Der Does DM, Karachaliou E, Sakimura K, Penn AC (2022a) Common synaptic phenotypes arising from diverse mutations in the human NMDA receptor subunit GluN2A. Commun Biol 5:174.

Elmasri M, Lotti JS, Aziz W, Steele OG, Karachaliou E, Sakimura K, Hansen KB, Penn AC (2022b) Synaptic dysfunction by mutations in GRIN2B: influence of triheteromeric NMDA receptors on gain-of-function and loss-of-function mutant classification. Brain Sci 12:789.

Erreger K, et al. (2007) Subunit-specific agonist activity at NR2A-, NR2B-, NR2C-, and NR2D-containing *N*-methyl-ᴅ-aspartate glutamate receptors. Mol Pharmacol 72:907–920.

Erreger K, Dravid SM, Banke TG, Wyllie DJ, Traynelis SF (2005) Subunit-specific gating controls rat NR1/NR2A and NR1/NR2B NMDA channel kinetics and synaptic signalling profiles. J Physiol 563:345–358.

Gambrill AC, Barria A (2011) NMDA receptor subunit composition controls synaptogenesis and synapse stabilization. Proc Natl Acad Sci U S A 108:5855–5860.

Garcia-Nafria J, Watson JF, Greger IH (2016) IVA cloning: a single-tube universal cloning system exploiting bacterial in vivo assembly. Sci Rep 6:27459.

Gray JA, Shi Y, Usui H, During MJ, Sakimura K, Nicoll RA (2011) Distinct modes of AMPA receptor suppression at developing synapses by GluN2A and GluN2B: single-cell NMDA receptor subunit deletion in vivo. Neuron 71:1085–1101.

Hall BJ, Ripley B, Ghosh A (2007) NR2B signaling regulates the development of synaptic AMPA receptor current. J Neurosci 27:13446–13456.

Hansen KB, et al. (2021) Structure, function, and pharmacology of glutamate receptor ion channels. Pharmacol Rev 73:298–487.

Hansen KB, Ogden KK, Yuan H, Traynelis SF (2014) Distinct functional and pharmacological properties of triheteromeric GluN1/GluN2A/GluN2B NMDA receptors. Neuron 81:1084–1096.

Hanson JE, Yuan H, Perszyk RE, Banke TG, Xing H, Tsai MC, Menniti FS, Traynelis SF (2024) Therapeutic potential of *N*-methyl-D-aspartate receptor modulators in psychiatry. Neuropsychopharmacology 49:51–66.

Hattier MA, Matson JL, Belva BC, Horovitz M (2011) The occurrence of challenging behaviours in children with autism spectrum disorders and atypical development. Dev Neurorehabil 14:221–229.

Hatton CJ, Paoletti P (2005) Modulation of triheteromeric NMDA receptors by N-terminal domain ligands. Neuron 46:261–274.

Horak M, Petralia RS, Kaniakova M, Sans N (2014) ER to synapse trafficking of NMDA receptors. Front Cell Neurosci 8:394.

Hu C, Chen W, Myers SJ, Yuan H, Traynelis SF (2016) Human GRIN2B variants in neurodevelopmental disorders. J Pharmacol Sci 132:115–121.

Huettner JE, Bean BP (1988) Block of *N*-methyl-D-aspartate-activated current by the anticonvulsant MK-801: selective binding to open channels. Proc Natl Acad Sci U S A 85:1307–1311.

Humphrey W, Dalke A, Schulten K (1996) VMD: visual molecular dynamics. J Mol Graph 14:33.

Ishihama Y, Rappsilber J, Mann M (2006) Modular stop and go extraction tips with stacked disks for parallel and multidimensional peptide fractionation in proteomics. J Proteome Res 5:988–994.

Jahr CE (1992) High probability opening of NMDA receptor channels by L-glutamate. Science 255:470–472.

Jo S, Kim T, Iyer VG, Im W (2008) CHARMM-GUI: a web-based graphical user interface for CHARMM. J Comput Chem 29:1859–1865.

Karakas E, Furukawa H (2014) Crystal structure of a heterotetrameric NMDA receptor ion channel. Science 344:992–997.

Kellermayer B, et al. (2018) Differential nanoscale topography and functional role of GluN2-NMDA receptor subtypes at glutamatergic synapses. Neuron 100:106.

Kiryk A, Janusz A, Zglinicki B, Turkes E, Knapska E, Konopka W, Lipp HP, Kaczmarek L (2020) IntelliCage as a tool for measuring mouse behavior - 20 years perspective. Behav Brain Res 388:112620.

Kobayashi Y, et al. (2013) Genetic dissection of medial habenula-interpeduncular nucleus pathway function in mice. Front Behav Neurosci 7:17.

Korinek M, et al. (2015) Cholesterol modulates open probability and desensitization of NMDA receptors. J Physiol 593:2279–2293.

Kuchtiak V, Smejkalova T, Horak M, Vyklicky L, Balik A (2024) Analysis of surface expression of NMDAR subunits in primary hippocampal neurons. In: *NMDA receptors: methods in molecular biology* (Burnashev N, Szepetowski P, eds), pp 29–46. New York: Humana.

Kulak NA, Geyer PE, Mann M (2017) Loss-less nano-fractionator for high sensitivity, high coverage proteomics. Mol Cell Proteomics 16:694–705.

Kulesskaya N, Voikar V (2014) Assessment of mouse anxiety-like behavior in the light–dark box and open-field arena: role of equipment and procedure. Physiol Behav 133:30–38.

Kutsuwada T, et al. (1996) Impairment of suckling response, trigeminal neuronal pattern formation, and hippocampal LTD in NMDA receptor epsilon 2 subunit mutant mice. Neuron 16:333–344.

Kysilov B, Hrcka Krausova B, Vyklicky V, Smejkalova T, Korinek M, Horak M, Chodounska H, Kudova E, Cerny J, Vyklicky L (2022) Pregnane-based steroids are novel positive NMDA receptor modulators that may compensate for the effect of loss-of-function disease-associated GRIN mutations. Br J Pharmacol 179:3970–3990.

Ladislav M, Cerny J, Krusek J, Horak M, Balik A, Vyklicky L (2018) The LILI motif of M3-S2 linkers is a component of the NMDA receptor channel gate. Front Mol Neurosci 11:113.

Laube B, Hirai H, Sturgess M, Betz H, Kuhse J (1997) Molecular determinants of agonist discrimination by NMDA receptor subunits: analysis of the glutamate binding site on the NR2B subunit. Neuron 18:493–503.

Lazaridis T (2003) Effective energy function for proteins in lipid membranes. Proteins 52:176–192.

Le T, Zarsky V, Nyvltova E, Rada P, Harant K, Vancova M, Verner Z, Hrdy I, Tachezy J (2020) Anaerobic peroxisomes in *Mastigamoeba balamuthi*. Proc Natl Acad Sci U S A 117:2065–2075.

Lee J, Cheng X, Swails JM, Yeom MS, Eastman PK, Lemkul JA, Wei S, Buckner J, Jeong JC, Qi Y (2016) CHARMM-GUI input generator for NAMD, GROMACS, AMBER, OpenMM, and CHARMM/OpenMM simulations using the CHARMM36 additive force field. J Chem Theory Comput 12:405–413.

Lee C-H, Lü W, Michel JC, Goehring A, Du J, Song X, Gouaux E (2014) NMDA receptor structures reveal subunit arrangement and pore architecture. Nature 511:191–197.

Liu S, Zhou L, Yuan H, Vieira M, Sanz-Clemente A, Badger JD 2nd, Lu W, Traynelis SF, Roche KW (2017) A rare variant identified within the GluN2B C-terminus in a patient with autism affects NMDA receptor surface expression and spine density. J Neurosci 37:4093–4102.

Luo J, Wang Y, Yasuda RP, Dunah AW, Wolfe BB (1997) The majority of *N*-methyl-D-aspartate receptor complexes in adult rat cerebral cortex contain at least three different subunits (NR1/NR2A/NR2B). Mol Pharmacol 51:79–86.

Masuda T, Tomita M, Ishihama Y (2008) Phase transfer surfactant-aided trypsin digestion for membrane proteome analysis. J Proteome Res 7: 731–740.

Mayes SD, Becker SP, Calhoun SL, Waschbusch DA (2023) Comparison of the cognitive disengagement and hypoactivity components of sluggish cognitive tempo in autism, ADHD, and population-based samples of children. Res Child Adolesc Psychopathol 51:47–54.

McAlister GC, Nusinow DP, Jedrychowski MP, Wuhr M, Huttlin EL, Erickson BK, Rad R, Haas W, Gygi SP (2014) Multinotch MS3 enables accurate, sensitive, and multiplexed detection of differential expression across cancer cell line proteomes. Anal Chem 86:7150–7158.

Mennerick S, Zorumski CF (1995) Paired-pulse modulation of fast excitatory synaptic currents in microcultures of rat hippocampal neurons. J Physiol 488:85–101.

Philpot BD, Weisberg MP, Ramos MS, Sawtell NB, Tang YP, Tsien JZ, Bear MF (2001) Effect of transgenic overexpression of NR2B on NMDA receptor function and synaptic plasticity in visual cortex. Neuropharmacology 41:762–770.

Platzer K, et al. (2017) GRIN2B encephalopathy: novel findings on phenotype, variant clustering, functional consequences and treatment aspects. J Med Genet 54:460–470.

Rauner C, Kohr G (2011) Triheteromeric NR1/NR2A/NR2B receptors constitute the major *N*-methyl-D-aspartate receptor population in adult hippocampal synapses. J Biol Chem 286:7558–7566.

Rosenmund C, Feltz A, Westbrook GL (1995) Synaptic NMDA receptor channels have a low open probability. J Neurosci 15:2788–2795.

Sauer AK, Hagmeyer S, Grabrucker AM (2022) Prenatal zinc deficient mice as a model for autism spectrum disorders. Int J Mol Sci 23:6082.

Sceniak MP, Fedder KN, Wang Q, Droubi S, Babcock K, Patwardhan S, Wright-Zornes J, Pham L, Sabo SL (2019) An autism-associated mutation in GluN2B prevents NMDA receptor trafficking and interferes with dendrite growth. J Cell Sci 132:jcs232892.

Scherer MK, Trendelkamp-Schroer B, Paul F, Perez-Hernandez G, Hoffmann M, Plattner N, Wehmeyer C, Prinz JH, Noe F (2015) PyEMMA 2: a software package for estimation, validation, and analysis of Markov models. J Chem Theory Comput 11:5525–5542.

Schymkowitz J, Borg J, Stricher F, Nys R, Rousseau F, Serrano L (2005) The FoldX web server: an online force field. Nucleic Acids Res 33:W382–W388.

Serraz B, Grand T, Paoletti P (2016) Altered zinc sensitivity of NMDA receptors harboring clinically-relevant mutations. Neuropharmacology 109: 196–204.

Sheng M, Cummings J, Roldan LA, Jan YN, Jan LY (1994) Changing subunit composition of heteromeric NMDA receptors during development of rat cortex. Nature 368:144–147.

Shin W, et al. (2020) Early correction of synaptic long-term depression improves abnormal anxiety-like behavior in adult GluN2B-C456Y-mutant mice. PLoS Biol 18:e3000717.

Smejkalova T, Korinek M, Krusek J, Hrcka Krausova B, Candelas Serra M, Hajdukovic D, Kudova E, Chodounska H, Vyklicky L (2021) Endogenous neurosteroids pregnanolone and pregnanolone sulfate potentiate presynaptic glutamate release through distinct mechanisms. Br J Pharmacol 178:3888–3904.

Sprengel R, et al. (1998) Importance of the intracellular domain of NR2 subunits for NMDA receptor function in vivo. Cell 92:279–289.

Stiedl O, Radulovic J, Lohmann R, Birkenfeld K, Palve M, Kammermeier J, Sananbenesi F, Spiess J (1999) Strain and substrain differences in context- and tone-dependent fear conditioning of inbred mice. Behav Brain Res 104:1–12.

Stroebel D, Carvalho S, Grand T, Zhu SJ, Paoletti P (2014) Controlling NMDA receptor subunit composition using ectopic retention signals. J Neurosci 34:16630–16636.

Stroebel D, Casado M, Paoletti P (2018) Triheteromeric NMDA receptors: from structure to synaptic physiology. Curr Opin Physiol 2:1–12.

Swanger SA, et al. (2016) Mechanistic insight into NMDA receptor dysregulation by rare variants in the GluN2A and GluN2B agonist binding domains. Am J Hum Genet 99:1261–1280.

Tarabeux J, et al. (2011) Rare mutations in *N*-methyl-D-aspartate glutamate receptors in autism spectrum disorders and schizophrenia. Transl Psychiatry 1:e55.

Tovar KR, McGinley MJ, Westbrook GL (2013) Triheteromeric NMDA receptors at hippocampal synapses. J Neurosci 33:9150–9160.

Tovar KR, Westbrook GL (1999) The incorporation of NMDA receptors with a distinct subunit composition at nascent hippocampal synapses in vitro. J Neurosci 19:4180–4188.

Turecek R, Vlcek K, Petrovic M, Horak M, Vlachova V, Vyklicky L Jr (2004) Intracellular spermine decreases open probability of *N*-methyl-D-aspartate receptor channels. Neuroscience 125:879–887.

Tyanova S, Cox J (2018) Perseus: a bioinformatics platform for integrative analysis of proteomics data in cancer research. Methods Mol Biol 1711: 133–148.

UniProt C (2021) UniProt: the universal protein knowledgebase in 2021. Nucleic Acids Res 49:D480–D489.

Uzunova G, Hollander E, Shepherd J (2014) The role of ionotropic glutamate receptors in childhood neurodevelopmental disorders: autism spectrum disorders and fragile x syndrome. Curr Neuropharmacol 12: 71–98.

Vieira M, Yong XLH, Roche KW, Anggono V (2020) Regulation of NMDA glutamate receptor functions by the GluN2 subunits. J Neurochem 154: 121–143.

Vyklicky V, et al. (2018) Surface expression, function, and pharmacology of disease-associated mutations in the membrane domain of the human GluN2B subunit. Front Mol Neurosci 11:110.

Vyklicky V, Korinek M, Balik A, Smejkalova T, Krausova B, Vyklicky L (2016) Analysis of whole-cell NMDA receptor currents. In: *Ionotropic glutamate receptor technologies. Neuromethods* (Popescu G, ed) Vol. 106, pp. 205–219. New York, NY: Humana Press.

Wang CC, Held RG, Chang SC, Yang LL, Delpire E, Ghosh A, Hall BJ (2011) A critical role for GluN2B-containing NMDA receptors in cortical development and function. Neuron 72:789–805.

Webb B, Sali A (2014) Comparative protein structure modeling using MODELLER. Curr Protoc Bioinformatics 47:5.6.1–5.6.37.

White SW, Oswald D, Ollendick T, Scahill L (2009) Anxiety in children and adolescents with autism spectrum disorders. Clin Psychol Rev 29: 216–229.

Williams K (1993) Ifenprodil discriminates subtypes of the *N*-methyl-D-aspartate receptor: selectivity and mechanisms at recombinant heteromeric receptors. Mol Pharmacol 44:851–859.